CFD modeling of a fluidized bed with volatiles distributor for biomass chemical looping combustion combustion

Chemical Engineering Science 295 (2024) 120211

Contents lists available at ScienceDirect

Chemical Engineering Science

journal homepage: www.elsevier.com/locate/ces

CFD modeling of a fluidized bed with volatiles distributor for biomass chemical looping combustion

Xiaobao Wang [a,1], Xiaoyun Li [b,1], Lan Yi [a], Anders Lyngfelt [b], Tobias Mattisson [b], Xiaoqin Wu [a], Hao Luo [a,*], Qingang Xiong [c,*]

[a] School of Chemistry and Chemical Engineering, Hubei Key Laboratory of Coal Conversion and New Carbon Materials, Wuhan University of Science and Technology, Wuhan 430081, China
[b] Division of Energy Technology, Department of Space, Earth and Environment, Chalmers University of Technology, 412 96 Gothenburg, Sweden
[c] State Key Laboratory of Pulp and Paper Engineering, South China University of Technology, Guangzhou 510640, China

ARTICLE INFO

Keywords:
Biomass chemical looping combustion
Fluidized bed
Volatiles distributor
Process intensification
CFD

ABSTRACT

Achieving high volatiles conversion is crucial to biomass chemical looping combustion. Challenges arise from rapid devolatilization of biomass and limited biomass injection ports, resulting in volatiles with insufficient contact with oxygen carriers in fluidized beds. A concept called volatiles distributor (VD) has recently been proposed and investigated in a cold-flow fluidized bed, which shows excellent performance in achieving an even distribution of volatiles over the cross section. To deeply understand VD's impact on hydrodynamics behaviors, pioneering three-dimensional full-loop cold-flow CFD simulations were conducted using an Eulerian multiphase granular model. Three drag models, i.e., Gidaspow, Filtered, and two-step EMMS/bubbling, were evaluated against experimental data. While all models perform well in bubbling fluidization, the two-step EMMS/bubbling model excels in turbulent fluidization. Additionally, CFD simulations reveal improved mixing between volatiles and bed materials with VD, highlighting its efficiency in addressing incomplete conversion of high-volatile fuels like biomass in fluidized bed systems.

1. Introduction

As a CO_2-negative emission technique, Bio-Energy Carbon Capture and Storage (BECCS) technology has been considered as one of the most promising methods for achieving the climate target (Masson-Delmotte et al., 2021). However, the cost of BECCS is highly dependent on CO_2 concentration in emission gas. In traditional biomass combustion processes, CO_2 concentration from the combustor outlet is rather low (<20 %) and mixed with other gas species (such as N_2, CO, and O_2). Therefore, the cost of BECCS significantly reduces the economic profitability of plants. In contrast to traditional biomass combustion processes, chemical looping combustion uses oxygen-carrier particles to transfer oxygen between two interconnected fluidized beds (Shao et al., 2020), i.e., from air reactor to biomass reactor. An essentially pure stream of CO_2 can be generated assuming fully converted combustible gases with oxygen carriers in a biomass reactor. Thus, inherent carbon capture can be achieved without a high energy penalty for gas separation (Daneshmand-Jahromi et al., 2023; Qasim et al., 2022; Yan et al., 2022). However, due to the fast devolatilization of biomass and limited biomass injection ports, local upwards streams of volatiles near injection ports can be expected, which would cause limited contact between volatiles and oxygen carriers, and hence poor volatiles conversion (Berdugo Vilches et al., 2017).

It has been observed that fuel conversion in fuel reactors can be significantly enhanced by employing oxygen carriers capable of releasing oxygen in gas phase, a process known as chemical looping with oxygen uncoupling (CLOU). This includes Cu-based (Arjmand et al., 2011; Gayán et al., 2012; Krzywanski et al., 2022; Skulimowska et al., 2017), Mn-based (Azimi et al., 2013; Lyngfelt et al., 2023; Shulman et al., 2009), and perovskite-type (Abad et al., 2019; Larring et al., 2020; Liu et al., 2022; Moldenhauer et al., 2020) oxygen carriers synthesized using various supported materials and techniques, in contrast to traditional oxygen carriers like ilmenite used in regular CLC processes (Hedayati et al., 2022; Rydén et al., 2010; Zylka et al., 2020). However, transitioning from small pilots to large-scale operations involves a substantial increase in cross-sectional area of fluidized beds. This

* Corresponding authors.
E-mail addresses: haoluo@wust.edu.cn (H. Luo), qingangxiong@scut.edu.cn (Q. Xiong).
[1] These authors contributed equally to this work.

https://doi.org/10.1016/j.ces.2024.120211
Received 25 February 2024; Received in revised form 28 April 2024; Accepted 30 April 2024
Available online 2 May 2024

enlargement can significantly intensify local plume of volatiles over fuel entry, resulting in reduced contact between volatiles and oxygen carriers. Therefore, merely developing CLOU oxygen carriers may not be sufficient to address conversion of volatiles in fuel reactors, especially in large-scale applications. Moreover, drawbacks associated with CLOU oxygen carriers, such as susceptibility to sintering and agglomeration, limited mechanical strength, slow oxidation kinetics, and potential deactivation due to fuel impurities and high production costs, may make CLOU oxygen carriers not attractive for all large-scale implementations.

Hence, improvements on fuel reactor designs can also be considered to enhance conversion of volatiles. When comparing various fuel feeding positions, specifically above-bed and in-bed methods, it was observed that the in-bed fuel feeding approach enhances contact between volatiles and oxygen carriers (Linderholm et al., 2012). Therefore, a more uniform distribution of volatiles over cross section of biomass reactors at positions as low as possible will enhance contact between volatiles and oxygen-carrier particles, thus improving volatiles' conversion. However, it is challenging to add more in-bed fuel feeding systems over the cross-section of the industrial-level fluidized-bed. Various types of internals were proposed and subsequently demonstrated to enhance the gas–solid contact and fuel conversion within the fuel reactor (Guío-Pérez et al., 2014; Pérez-Vega et al., 2019). Nevertheless, there is no specific design found for the lateral distribution of the local plume of volatiles over fuel entry of the fuel reactor. Given that the fuel reactor typically operates as bubbling fluidized bed, resulting in a concentration of the oxygen carriers at the bottom of the reactor, the objective is to achieve a uniform cross-sectional distribution of volatiles at the lowest feasible position. For such reasons, the concept of volatiles distributor (VD) has been proposed, and preliminary experimental studies have proved that VD is a straightforward and effective choice to regulate lateral gas distribution in biomass reactor (Li et al., 2022a; Li et al., 2021; Li et al., 2022b). In general, VD is a downward opened box configured as an arm located at bottom of a fluidized bed with distribution holes on both sides to modify lateral gas distribution, as illustrated in Fig. 1 (Li et al., 2021). Due to limited open area and different arrangements of distribution holes on both sides, VD allows for volatiles to spread along length of VD, and equipping VD with internal baffles may improve lateral gas distribution further (Li et al., 2022a). But on the other hand, the introduction of VD would inevitably modify hydrodynamics, and heat and mass transfer characteristics of fluidized beds. Hence, in-depth understanding of the intrinsic characteristics of fluidized beds with VD is the prerequisite to efficient utilization of VD for achieving uniform distribution of volatiles. As transport phenomena in a fluidized bed with VD is usually complex, it would be costly and time-consuming to clarify the intrinsic characteristics of fluidized beds with VD solely by experimental approaches.

With the fast development of computational capacity, computational fluid dynamics (CFD) has been widely viewed as an indispensable complement of experiments to investigate the effect of internal structures of fluidized beds (Li and Huang, 2018; Lu et al., 2016; Samruamphianskun et al., 2012). Among all mainstream CFD models for fluidized beds, the Eulerian-Eulerian (E-E) model has been mostly used as it requires much less computational resources (Luo et al., 2022; Sundaresan et al., 2018). Thus, it is reasonable to use the E-E model to clarify the intrinsic characteristics of fluidized beds with VD for biomass chemical looping combustion. But on the other hand, modeling accuracy of the E-E model is highly dependent on the chosen drag models (Du et al., 2022; Luo et al., 2017; Milioli and Milioli, 2023; Sarkar et al., 2016; Stamatopoulos et al., 2023; Zhu et al., 2019). Till date, there are mainly three types of drag models for use in the E-E model, i.e., homogeneous drag models where the Gidaspow model (Gidaspow, 1994) is the representative, filtered drag models (Igci et al., 2008), and variational drag models with the energy-minimization multi-scale (EMMS) model (Luo et al., 2017; Wang and Li, 2007) as the representative. Though each type of drag models has shown their advantages in respective E-E modeling of fluidized beds, their applicability has not been clarified in E-E modeling of fluidized beds with VD for biomass chemical looping combustion. Therefore, this study first aims to identify the best drag model to be used in E-E modeling of fluidized beds with VD for biomass chemical looping combustion, and then use the identified drag model to investigate the effects of VD on transport phenomena and reactions of fluidized-bed biomass chemical looping combustion.

In this work, a comprehensive comparison of three different drag models, i.e., the Gidaspow model(Gidaspow, 1994), the filtered model proposed by Sarkar (Sarkar et al., 2016), and the two-step EMMS/bubbling model (Luo et al., 2017), was conducted first to show their prediction of distributions of solids volume fraction, pressure, volatiles, etc., in E-E modeling of a fluidized-bed biomass chemical looping combustor. With the identified most suitable drag model, the effects of VD on physicochemical performance of the fluidized-bed biomass chemical looping combustor were fully investigated to support design, optimization, and scale-up of fluidized-bed biomass chemical looping combustion.

2. Experiments for model validation

Cold-flow experiments of a circulating fluidized bed (CFB) with VD

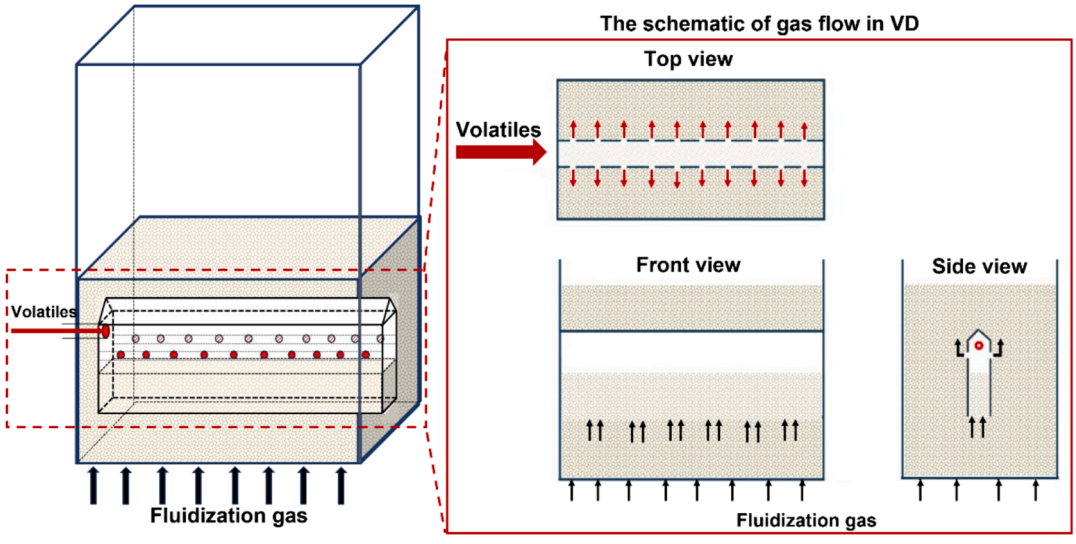

Fig. 1. Illustration of VD as a downward open box immersed at the bottom of fluidized bed with side holes.

were conducted for model validation, as shown in Fig. 2. The CFB consists of a wind box, a riser, a cyclone, and a return leg. There is a perforated plate between the wind box and riser for primary air, which has 1660 holes of 2 mm diameter, corresponding to 6.2 % opening area of the cross section. The gas supply system includes primary air for fluidization in the riser, inlet air at bottom of the return leg to maintain solids flow in the recycle loop, and secondary air mixed with tracer gas, i.e., CO_2, to simulate volatiles injected from left bottom of the riser. Height and cross-sectional dimensions of the riser are 8500 mm and 700 mm × 120 mm. There are 58 distribution holes with diameter of 5 mm on the VD. The VD is installed at bottom of the riser on its front plate with bolts and nuts. Gas injected into the VD can mix with fluidization gas and leaves the VD through the distribution holes. Depending on pressure drop over the holes, part of injected gas may leave the VD through its bottom.

Measurement system of the experiments includes 24 pressure measurement taps along the riser for determination of vertical solids distribution, and a X-STREAM Enhanced XEGK gas analyzer used to measure gas concentration at bottom of the riser. Piezo resistive pressure transducers were used for pressure measurement. Most of the pressure transducers measure vertical differential pressure between two pressure taps in order to achieve high accuracy. Transducers with varying measurement ranges, spanning from 5 mbar to 200 mbar, were utilized corresponding to different heights of pressure measurement taps. Instrumental error associated with these transducers is 1 %. Average values over 120 s period at these different positions under each condition were used to estimate pressure over the whole cross-section. Two sets of gas sampling tubes, i.e., HSV 1–6 and LSV 1–6, are installed at bottom of the riser, as indicated in Fig. 2. The HSV 1–6 is used to measure horizontal distribution of the simulated volatiles, and the LSV 1–6 is used to detect if there is any leakage of the simulated volatiles from bottom of the VD. The gas sampling tube including 10 mm filters on the top penetrates 70 mm and 50 mm, respectively, into the bed without and with VD. The corresponding sampling points were selected in the CFD simulations for comparison with experimental data. The gas sample flows continuously at 1 L/min into the gas analyzer via filters, which means that gas is continuously pumped out from the fluidized bed. Measurement range of the tracer gas CO_2 in the gas analyzer is 100 to 10000 ppm with both zero-point and span drifts related to full scale as 1 %. CO_2 concentration of each gas sampling tube was measured and recorded at 1 Hz during 120 s, with 90 s stabilization time before data was recorded. When the data were analyzed, averaged value was taken during the 120 s period. It should be noted that uncertainty of gas concentration measurements by suction probes in lower part of the fluidized bed might increase due to considerable bypass flows at higher fluidization velocities (Lyngfelt et al., 1996).

Bed materials used in the experiments are glass beads with bulk density of 2600 kg/m^3 and average particle size of 316 μm, which belong to the Geldart's group B classification (Geldart, 1973). Under ambient conditions, minimum fluidization velocity of the glass beads is 0.067 m/s, and terminal velocity is 2.21 m/s (Karlsson et al., 2017). Solids inventory of each experiment is 100 kg. Two series of experiments with and without VD were performed. The first series serve as reference cases and focus on horizontal distribution of simulated volatiles in the fluidized bed with varying superficial gas velocities without VD. $V_{SV}/(V_{air} + V_{SV})$ (Notations can be seen in Table 1) was set to approximately 10 % to keep almost the same percentage of simulated volatiles under different fluidization velocities. The second series aim to provide experimental data under different fluidization velocities and simulate volatiles' percentages (approximately 10 %, 20 %, and 30 % at around 1 m/s of fluidization velocity) with VD. An overview of the experimental conditions is summarized in Table 1. Physical properties of the gases are given in Table S1 in the Supplementary Materials, which are determined by the DIPPR correlations (https://dippr.aiche.org/).

To assess lateral distribution of simulated volatiles under different operational conditions, an indicator of CO_2 concentration ratio (R) is

Table 1
An overview of the experimental conditions.

Case	U_g	Temperature	V_{air}	V_{SV}	CO_2 in SV	O_2 in SV
	(m/s)	(℃)	(Nm^3/h)	(Nm^3/h)	(%)	(%)
Experiments without VD						
1	0.94	30.78	235	20	1.72	20.59
2	2.04	40.04	474	64	1.09	20.73
3	3.09	41.45	717	94	1.11	20.72
4	4.13	42.15	967	114	1.09	20.73
Experiments with VD						
5	0.94	32.18	234	19	1.81	20.58
6	1.10	36.86	233	61	1.28	20.69
7	1.27	39.09	235	102	1.22	20.70
8	2.04	39.01	476	65	1.07	20.73
9	3.08	41.47	717	92	1.14	20.72
10	4.13	42.66	967	112	1.22	20.70

Note: U_g: superficial gas velocity; V_{air}: volumetric flow rate of primary air; V_{SV}: volumetric flow rate of simulated volatiles.

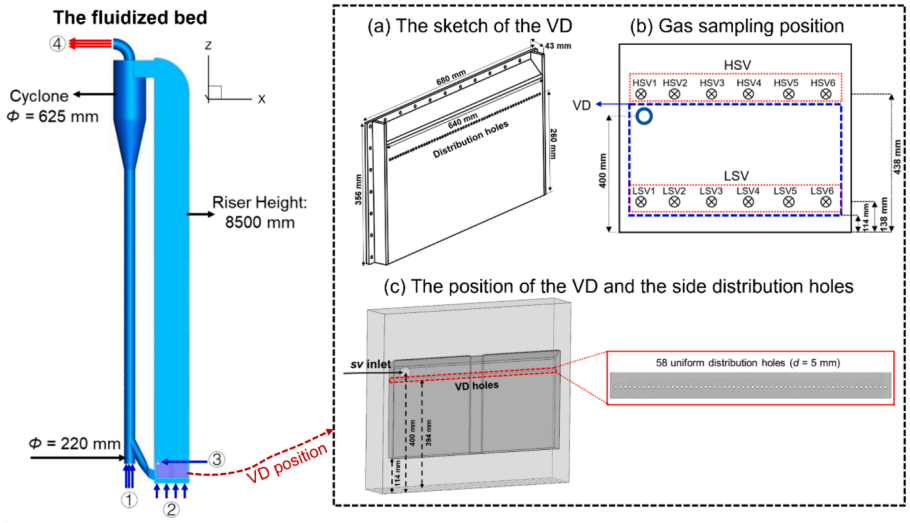

Fig. 2. Principal layout of the CFB cold-flow experimental setup and the sketch of the VD and gas sampling positions. (1) inlet of cyclone (2) inlet of primary air (3) inlet of simulated volatiles (4) outlet of cyclone.

defined as the ratio of CO_2 concentration measured by the gas analyzer at different horizontal positions to theoretically calculated average CO_2 concentration over the cross-section of the fluidized bed as

$$R = \frac{C_{CO2}}{C_{cal}} \tag{1}$$

$$C_{cal} = \frac{MF_{CO2}}{MF_{air} + MF_{SV} + MF_{CO2}} \tag{2}$$

Where C_{CO2} represents averaged CO_2 concentration (ppm) measured by the gas analyzer or predicted by the CFD simulations, and C_{cal} denotes expected average CO_2 concentration in cross-section of the fluidized bed if all gases are mixed ideally. MF_{CO2}, MF_{air}, and MF_{SV} are flowrates of CO_2 as a tracer gas, primary air, and simulated volatiles, respectively.

To quantitatively evaluate performance of the CFD simulations, mean relative error (MRE) and mean absolute error (MAE) are introduced in Eq. (3) and Eq. (4), respectively.

$$MRE = \frac{\frac{1}{N}\sum_{i=1}^{N}\left|Y_{CFD,i} - Y_{EXP,i}\right|}{\frac{1}{N}\sum_{i=1}^{N}\left(Y_{EXP,i}\right)} \tag{3}$$

$$MAE = \frac{1}{N}\sum_{i=1}^{N}\left|Y_{CFD,i} - Y_{EXP,i}\right| \tag{4}$$

Where Y_{CFD} and Y_{EXP} are values predicted by CFD simulations and measured by experiments, respectively. N is the total number of sample points. For pressure, N is 24. For CO_2 concentration at HSV and LSV, N is 6. The subscript i is the i^{th} sample point.

3. Model description and simulation settings

The Eulerian multi-phase granular model in the ANSYS Fluent 2023R1 was employed in this work. Governing equations of the Eulerian multi-phase granular model are given in Table S2 in the Supplementary Materials. The study considers three different drag models. The Gidaspow (Gidaspow, 1994) and filtered models (Sarkar et al., 2016) are available in ANSYS Fluent 2023R1, and the two-step EMMS/bubbling model (Luo et al., 2017) was implemented by the User Defined Functions (UDFs). Detailed descriptions of the three models are given in **Section 3.1-3.3**. The kinetic theory of granular flow (KTGF) (Gidaspow et al., 1991) was used as closures for solids stress and viscosity for the Gidaspow model and two-step EMMS/bubbling model. For the filtered model (Sarkar et al., 2016), solids stress and viscosity are described by the filtered model instead of KTGF, as shown in Table S3 in the Supplementary Materials. No-slip and partial-slip boundary conditions were prescribed for the gas phase and solids phase, respectively. The standard k-ε turbulence model was used to describe turbulent flows (Benzarti et al., 2021; Ding et al., 2020; Zhang et al., 2017). As the standard k-ε requires less computational cost but gives reasonable prediction. The dispersed formulation of turbulence model was selected, as densities of gas and solid phase are significantly different (ANSYS, 2023). Density, viscosity, and mass diffusivity of the gas mixture are determined by the volume-averaged mixing law, mass-weighted mixing law, and kinetic theory, respectively.

Three-dimensional full-loop cold-flow simulation was adopted, as full-loop simulation can give more reasonable results as compared to single fluidized-bed simulation (Li et al., 2014; Lu et al., 2013; Luo et al., 2019; Tu et al., 2022) and the cold-flow experiments were conducted. The primary air distributor is streamlined to 184 holes with a diameter of 6 mm, maintaining the same opening ratio as the original 1660 holes with a diameter of 2 mm. This simplification reduces the total mesh number from 4 million to approximately 412 and 560 thousand polyhedral meshes for the case with VD and without VD, resulting a significant reduction in computational time. The polyhedral mesh was adopted, because of good convergency and low computational cost. The meshing procedure along with a skew and orthogonal quality analysis of cells are given in **Section 3** in the Supplementary Materials. Maximum skewness (0.864 and 0.636 for the fluidized bed without VD and with VD, respectively) is smaller than 0.95 and minimum orthogonal quality is larger than 0.05 (0.301 and 0.300 for the fluidized bed without VD and with VD, respectively), indicating that quality of the mesh is quite good for CFD modeling (Krzywanski et al., 2020a; Krzywanski et al., 2020b). The corresponding average mesh size is about 61 and 55 times of the particle diameter, which is acceptable for the E-E modelling (Luo et al., 2017). Note that mesh size at bottom of the fluidized bed (0 ~ 0.6 m) is much finer than that at other locations, as performance of the VD in the dense bed is focused. In addition, a grid-dependent study given in the Supplementary Materials shows that mesh size has a weaker effect on the modeling results, where the case with 560 thousand polyhedral meshes gives almost the same pressure profiles and quite similar CO_2 concentration profile as that of the case with 810 thousand polyhedral meshes, which further confirms that the mesh used in this work is reasonable. Solids leaving outlet of the cyclone are recirculated to inlet of the recycle loop by the UDF to keep constant of solids inventory. Time step of 0.001 s and maximum iteration of 40 were chosen to ensure conservation of continuity, momentum, species transport, and turbulence with convergence of 10^{-3}. According to our preliminary simulations, quasi-steady state reaches after running 30 s of physical time. Therefore, all simulations of the fluidized bed with and without VD were run for 50 s and data of the last 20 s were collected for analysis. Settings of the CFD modeling are given in Table 2.

3.1. The Gidaspow model

The Gidaspow model (Gidaspow, 1994) is a combination of the Ergun equation (Ergun, 1952) and Wen-Yu model (Wen, 1966), which has been widely used to simulate fluidized beds operated in different flow regimes. For Geldart's Group B particles, a previous study showed that the Gidaspow model could give a reasonable prediction of bubbling fluidized beds, but failed to predict fast fluidized beds (Luo et al., 2019). Since the fluidized-bed system in this work can be operated under both bubbling and turbulent fluidization regimes, simulations with the Gidaspow model were carried out to evaluate its performance in these two fluidization regimes and then compared with other models. Formulation of the Gidaspow model is

$$\beta = \begin{cases} 0.75 C_{D0} \dfrac{\alpha_s \alpha_g \rho_g \left|\boldsymbol{u}_s - \boldsymbol{u}_g\right|}{d_s} \alpha_g^{-2.65} & (\alpha_g > 0.8) \\ 150 \dfrac{(1-\alpha_g)^2 \boldsymbol{u}_g}{\alpha_g d_s^2} + 1.75 \dfrac{\rho_g (1-\alpha_g)\left|\boldsymbol{u}_s - \boldsymbol{u}_g\right|}{d_s} & (\alpha_g \leqslant 0.8) \end{cases} \tag{5}$$

where

$$C_{D0} = \begin{cases} \dfrac{24\left(1 + 0.15 \mathrm{Re}_s^{0.687}\right)}{\mathrm{Re}_s} & (\mathrm{Re}_s < 1000) \\ 0.44 & (\mathrm{Re}_s \geqslant 1000) \end{cases} \tag{6}$$

Table 2
Simulation setting of the fluidized-bed system.

Unsteady formulation	Unsteady, First order implicit
Spatial discretization	Green-Gauss Cell based (ANSYS, 2023)
Pressure-Velocity Coupling	Phase Coupled SIMPLE (ANSYS, 2023)
Pressure	PRESTO! (ANSYS, 2023)
Momentum	Second Order Upwind
Volume Fraction	QUICK (ANSYS, 2023)
Turbulent Kinetic Energy	Second Order Upwind
Turbulent Dissipation Rate	First Order Upwind
Phase-1 CO_2	Second Order Upwind
Phase-1 O_2	Second Order Upwind
Angle of internal friction	30
Time step	0.001 s

$$\mathrm{Re}_s = \frac{\rho_g d_s \alpha_g |\boldsymbol{u}_s - \boldsymbol{u}_g|}{\mu_g} \tag{7}$$

Here, Re_s is Reynolds number. $\boldsymbol{u}_g$ and $\boldsymbol{u}_s$ are gas and solid velocities (m/s). α_g and α_s are volume fractions of gas and solids phase. ρ_g and ρ_s are gas and solid densities (kg/m^3). d_s is particle diameter (m). β is drag coefficient (kg/m^3/s). μ_g is gas dynamic viscosity (Pa·s). C_{D0} is the standard drag coefficient for a particle.

3.2. The filtered model

Formulation of the filtered model is given as

$$\beta = \frac{3}{4} C_{D0} \frac{\alpha_s \alpha_g \rho_g |\boldsymbol{u}_s - \boldsymbol{u}_g|}{d_s} \alpha_g^{-2.65} H_D \tag{8}$$

$$H_D = 1 - \min\left[\left(a + b/\left|u^*_{slip}\right|\right)\alpha_s^{c+d/\left|u^*_{slip}\right|}, 0.97\right] \tag{9}$$

where a, b, c, and d are given as

$$\begin{aligned} a &= 0.9506, \\ b &= 0.1708, \\ c &= 0.049\left(\frac{1}{\Delta^*_{filter}} - 1\right), \\ d &= 0.3358 \end{aligned} \tag{10}$$

and the expressions of u^*_{slip} and u_t are

$$u^*_{slip} = \frac{|\boldsymbol{u}_s - \boldsymbol{u}_g|}{u_t} \tag{11}$$

$$u_t = \frac{\boldsymbol{g} d_s^2 (\rho_s - \rho_g)}{18 \boldsymbol{u}_g} \tag{12}$$

where Δ^*_{filter} is dimensionless filtered size (Sarkar et al., 2016). $\boldsymbol{g}$ is the gravitational acceleration (m/s^2). Although the filtered model has exhibited its advantages in coarse-grid simulations of Geldart's Group A particles (Milioli and Milioli, 2023; Ozarkar et al., 2015; Sarkar et al., 2016), its applicability to Geldart's Group B particles is not very clear.

3.3. The two-step EMMS/bubbling model

In the two-step EMMS/bubbling model (Luo et al., 2017), heterogeneous index H_D is used as a binary function of Reynolds number and voidage. Thus, general expression of the two-step EMMS/bubbling model is the same as that of the filtered model (Luo et al., 2022). In contrast to the filtered model, inputs of the two-step EMMS/bubbling model are superficial gas velocity and physical properties of gas and solids phases. Thus, H_D is adjusted according to operating conditions of the simulated fluidized bed and physical properties of the gas and solids phases. As H_D varies with the encountered operating conditions, Fig. S8 shows the contour plot of H_D determined for different operating conditions. It is found that H_D with high superficial velocity $U_g = 4.13$ m/s is smaller than that with low superficial velocity, as sub-grid structures have pronounced effects on momentum transfer between gas and solids phases under higher superficial velocity (Luo et al., 2017; Shi et al., 2011). Fitted expressions of H_D in different cases are given in Table S6-S9 in the Supplementary Materials. Note that same H_D was used for cases with similar superficial gas velocity, as physical properties of gas and solids phases do not significantly change within a narrow range of temperature (absolute variation ≤ 50 °C), as shown in Table 1.

4. Results and discussion

4.1. Effects of drag models and validation

4.1.1. Fluidized bed without VD

Fig. 3 shows axial profiles of time-averaged solids volume fraction together with their contour plots. When $U_g = 0.94$ m/s, axial profiles of solids volume fraction and bed expansion predicted by the three models are almost the same. When $U_g = 2.04$ m/s, axial profiles of solids volume fraction predicted by the three models are slightly different. Although a transition region between the dense and dilute phases is captured by all models, bed expansion predicted by the Gidaspow model is the highest and that by the filtered model is the lowest. With the increase of U_g, axial profiles of solids volume fraction predicted by the three models become more different. Among the three models, the filtered model gives the lowest solids volume fraction for upper section of the fluidized bed but the highest for center section of the fluidized bed, while the two-step EMMS/bubbling model gives the highest solids volume fraction for bottom section of the fluidized bed.

Fig. 4 shows lateral profiles of time-averaged solids volume fraction at bed height of 0.4 m which is the same height as the injection of simulated volatiles. For the case of $U_g = 0.94$ m/s, results given by the three models are quite similar, and typical core-annulus structure where solids volume fraction is higher near wall and lower in central region, is captured. However, different models give quite different lateral profiles of time-averaged solids volume fraction when U_g is higher. It should be also noted that the filtered model fails to predict typical core-annulus structure when U_g is 2.04 m/s, 3.09 m/s, and 4.13 m/s, where there are two peaks close to wall. The reason is probably that special treatment of wall condition is not considered in the filtered model, but should be required for conditions with high U_g (Igci et al., 2011).

The comparison between experimental pressure data and predicted ones along riser height by the three drag models under different operating conditions is shown in Fig. 5. Note that pressure shown in this work is relative pressure. At low U_g, i.e., 0.94 m/s and 2.04 m/s, pressure profiles predicted by the three drag models are all in good agreement with the experimental data. With the increase of U_g, i.e., 3.09 m/s and 4.13 m/s, the two-step EMMS/bubbling model shows the best predictions. Although sub-grid structure is resolved, predicted pressures with the filtered model are still overestimated in most regions, which indicates higher solids volume fraction along riser height. As compared to the two-step EMMS/bubbling model, the Gidaspow model also overestimates pressures in the riser at higher U_g, which is consistent with our previous study (Luo et al., 2019).

To quantitatively evaluate model validation error on pressure, MRE and MAE between predicted pressure and experimental data are given in Table 3. At low U_g, i.e., 0.94 m/s and 2.04 m/s, MRE of the three models are smaller than 20 % and MAE of the three models are smaller than 0.4 kPa (smaller than 5 % of pressure difference between bottom and top of the riser), indicating good predictions of all models when the fluidized bed is operated at bubbling fluidization regime. With the increase of U_g, the two-step EMMS/bubbling model exhibits the lowest MRE (less than 20 %) and MAE (less than 0.4 kPa), whereas the filtered drag model shows MRE greater than 20 % and both the filtered and Gidaspow models have MAE values exceeding 0.4 kPa. In addition, absolute error of the filtered and Gidaspow models is over 0.8 kPa (approximate 10 % of pressure difference between bottom and top of the riser) in most of the region, as shown in Fig. S9 in the Supplementary Materials. These results indicate that the two-step EMMS/bubbling model has better performance in turbulent fluidization regime.

Lateral profiles of CO_2 concentration ratios at two different heights (HSV and LSV) predicted by the three drag models with experimental results under various operating conditions are shown in Fig. 6. All drag models give the same tendency of experiments, i.e., higher concentration ratio at left side for both LSV and HSV. At the LSV level, lateral profiles of CO_2 concentration ratio predicted by all drag models are

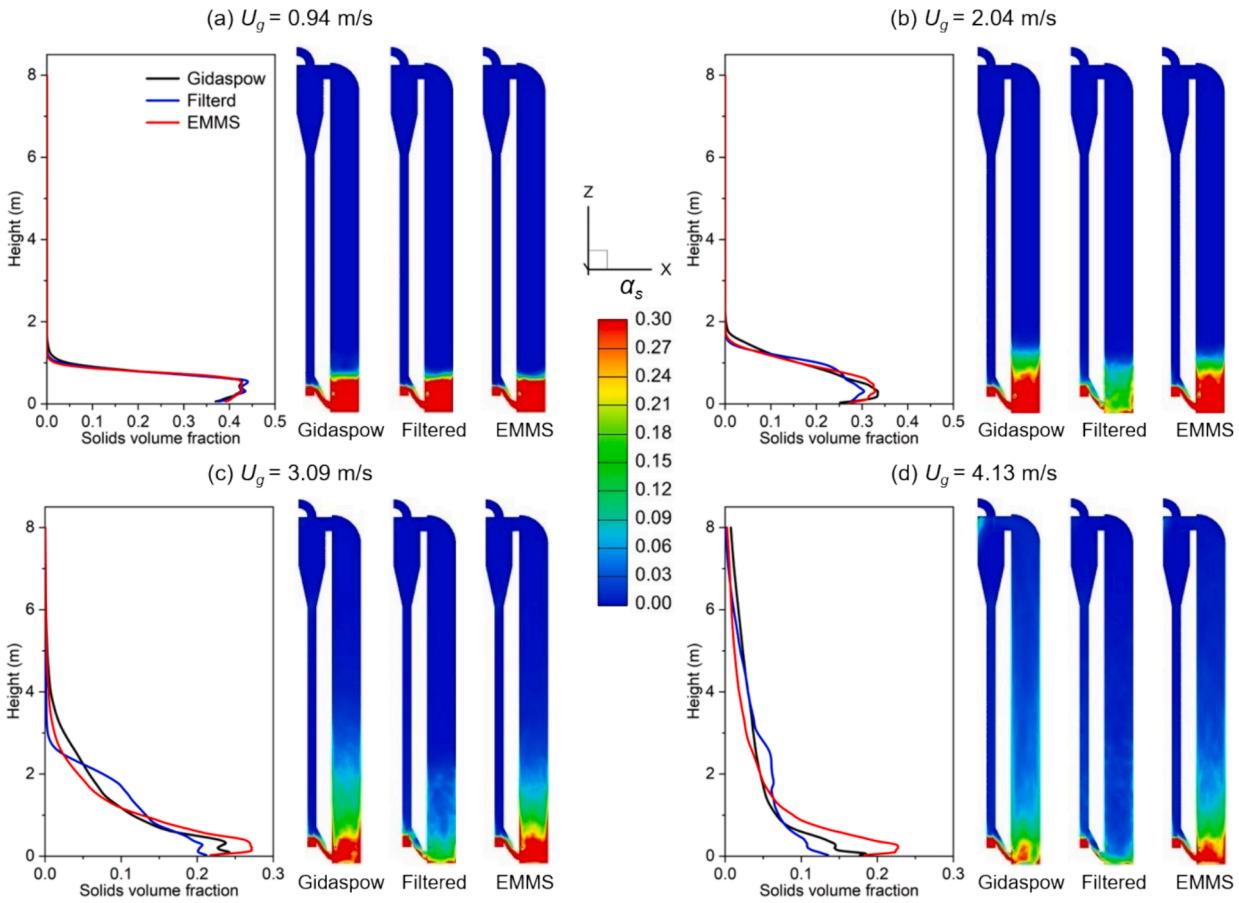

Fig. 3. Axial profiles of solids volume fraction in the fluidized bed without VD together with their contour plots predicted by the three drag models with different U_g ((a) U_g = 0.94 m/s, (b) U_g = 2.04 m/s, (c) U_g = 3.09 m/s, (d) U_g = 4.13 m/s).

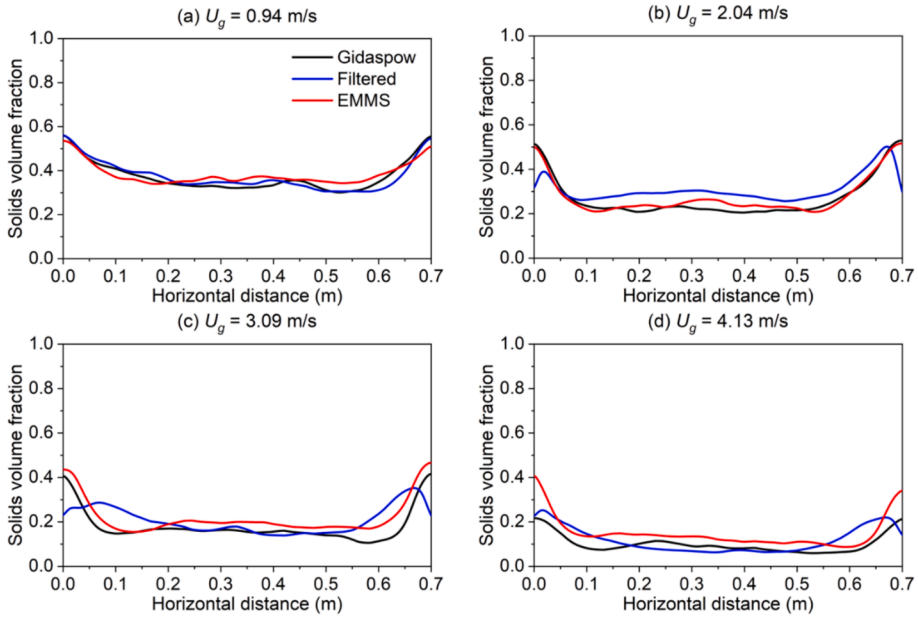

Fig. 4. Lateral profiles of solids volume fraction at bed height of 0.4 m without VD predicted by the three drag models with different U_g ((a) U_g = 0.94 m/s, (b) U_g = 2.04 m/s, (c) U_g = 3.09 m/s, (d) U_g = 4.13 m/s).

generally in good agreement with the experimental data. Both predicted and measured CO_2 concentration ratios at the LSV left side are much lower than that at the HSV left side. Since simulated volatiles are added 262 mm above the LSV level, the presence of CO_2 at the LSV level is explained by back mixing (Li et al., 2021). The deviation between CFD modeling and experimental data can be observed at U_g = 0.94 m/s,

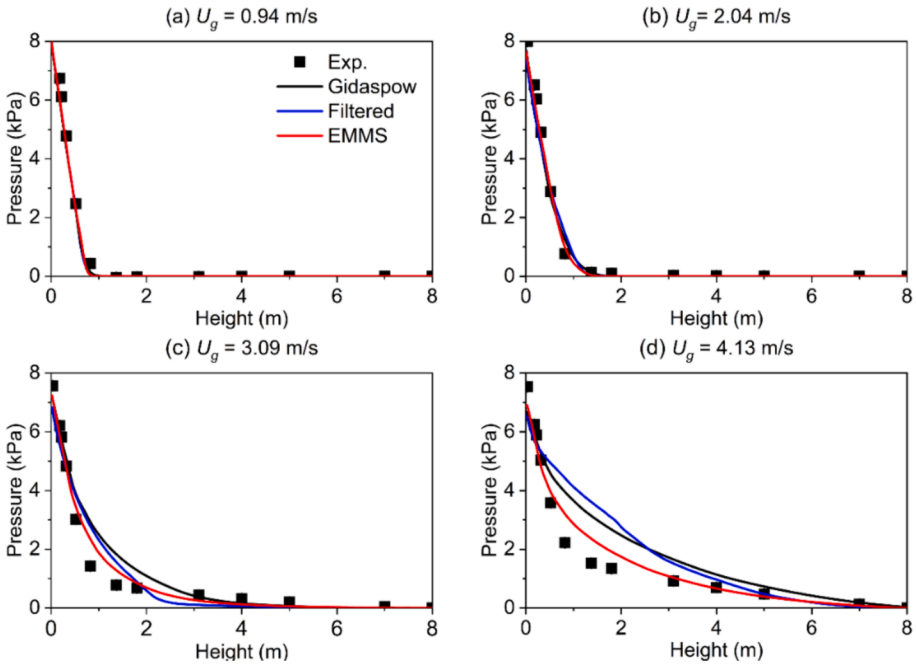

Fig. 5. Comparison of predicted axial pressure profiles without VD by using the three drag models with experimental data under different U_g ((a) $U_g = 0.94$ m/s, (b) $U_g = 2.04$ m/s, (c) $U_g = 3.09$ m/s, (d) $U_g = 4.13$ m/s).

Table 3
MRE and MAE between predicted pressure and experimental measurements.

Case	U_g (m/s)	MRE of pressure			MAE of pressure (kPa)		
		EMMS	Filtered	Gidaspow	EMMS	Filtered	Gidaspow
1	0.94	10.83 %	11.59 %	11.88 %	0.24	0.25	0.26
2	2.04	8.18 %	14.43 %	11.31 %	0.19	0.33	0.26
3	3.09	12.71 %	20.12 %	18.65 %	0.31	0.49	0.45
4	4.13	13.11 %	29.82 %	24.52 %	0.37	0.83	0.69

where the predicted CO_2 concentration ratio at the HSV level is underestimated except in the vicinity of the addition of simulated volatiles. The lower pressure drop over the air distributor at $U_g = 0.94$ m/s results in periodic, discontinuous, and large bubbles rising up in the center of bed, i.e., single bubble regime, which causes violent fluctuations of the bed and subsequently bring more simulated volatiles towards to the right side (Li et al., 2022a). Hence, more primary air for main fluidization would flow through the air distributor in the middle part at lower U_g in the experiments compared to the uniform velocity of primary air over the whole air distributor set in the CFD modeling. This could explain the underestimated CO_2 concentration ratios by CFD modeling at $U_g = 0.94$ m/s. For the other three operating conditions, the trends of lateral distributions of CO_2 concentration ratio predicted by the three drag models are generally consistent with the experimental data and performance of the two-step EMMS/bubbling model is slightly better than the other two.

To quantitatively evaluate model validation error on CO_2 concentration ratio, MRE and MAE between predicted CO_2 concentration ratio and experimental data are given in Tables 4 and 5. For all simulation cases, MRE is relatively large (over 20 %) and MAE of CO_2 concentration ratio at HSV is up to 1. However, it is important to note that average concentration of CO_2 as tracer gas in the fluidized bed reactor is rather low, i.e., 0.1 vol%. The discrepancy between predicted and experimental CO_2 concentration remains minimal, at less than 0.1 vol%, despite the relatively large MRE (e.g., 100 %) and MAE (e.g., 1.0) of CO_2 concentration ratio. More importantly, the trends of lateral profiles of CO_2 concentration ratio are well captured by all models, as shown in Fig. 6. Therefore, the results remain acceptable and can be used to analyze the effects of VD on gas–solid hydrodynamic behaviors.

Overall, all the three drag models have similar performance in the simulation of fluidized bed with lower U_g, i.e., bubbling fluidization regime, while the two-step EMMS/bubbling model gives the most reasonable results at $U_g = 3.04$ m/s, i.e., the transition regime from bubbling to turbulent, and $U_g = 4.13$ m/s, i.e., the turbulent regime. Therefore, the two-step EMMS/bubbling model is further used to evaluate its performance in CFD modeling of the fluidized bed with VD.

4.1.2. *Fluidized bed with VD*

Fig. 7 compares axial pressure profiles of the fluidized bed equipped with VD predicted by the two-step EMMS/bubbling model with experimental data. For the cases with lower superficial gas velocities, $U_g = 0.94$ m/s and 2.04 m/s, both experiments and CFD simulations show that pressure decreases rapidly with height of the fluidized bed and becomes zero at height of 0.9 m and 1.4 m, respectively. When U_g is 3.08 m/s and 4.13 m/s, both experiments and CFD simulations show that pressure decreases more slowly along the riser height, which means more particles are brought upwards with higher superficial gas velocity. In addition, MRE and MAE of pressure are smaller than 20 % and 0.4 kPa for most of the investigated cases, as shown in Table S10 and Table S11 in the Supplementary Materials. Generally, the CFD simulations are in good agreement with experimental data for all operating conditions, indicating that the two-step EMMS/bubbling model is applicable in both bubbling and turbulent fluidization regimes.

Fig. 8 shows both CFD predicted and measured lateral profiles of CO_2 concentration ratio at two different heights, HSV and LSV, with the VD inserted in the fluidized bed using various operating conditions. For

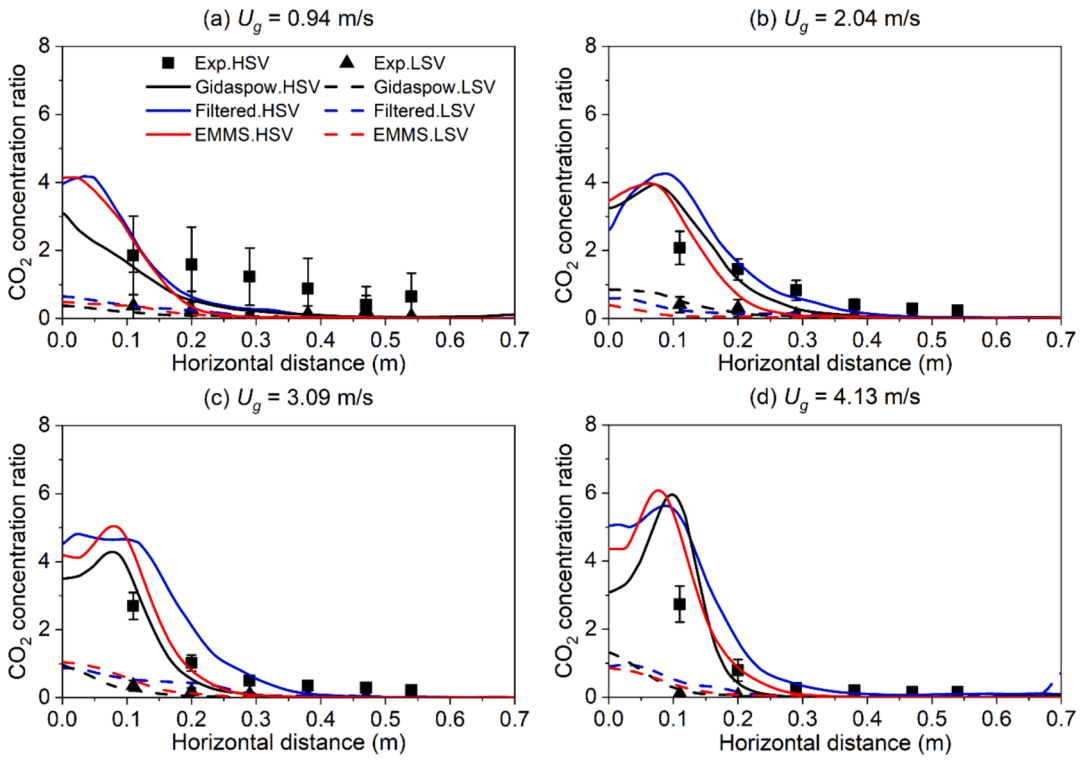

Fig. 6. Comparison of predicted lateral profiles of CO_2 concentration ratio at two different heights of the riser bottom (HSV: 0.483 m, LSV: 0.138 m) using the three drag models with experimental data under different U_g ((a) U_g = 0.94 m/s, (b) U_g = 2.04 m/s, (c) U_g = 3.09 m/s, (d) U_g = 4.13 m/s) without VD.

Table 4
MRE between predicted CO_2 concentration ratio and experimental measurement at HSV and LSV.

Case	U_g (m/s)	MRE of CO_2 concentration ratio at HSV			MRE of CO_2 concentration ratio at LSV		
		EMMS	Filtered	Gidaspow	EMMS	Filtered	Gidaspow
1	0.94	71.13 %	63.76 %	62.04 %	55.43 %	40.09 %	62.94 %
2	2.04	62.57 %	56.99 %	55.32 %	86.05 %	43.05 %	39.94 %
3	3.09	59.80 %	76.25 %	47.73 %	59.30 %	62.58 %	65.62 %
4	4.13	66.06 %	88.62 %	96.13 %	108.42 %	157.11 %	88.90 %

Table 5
MAE between predicted CO_2 concentration ratio and experimental measurement at HSV and LSV.

Case	U_g (m/s)	MAE of CO_2 concentration ratio at HSV			MAE of CO_2 concentration ratio at LSV		
		EMMS	Filtered	Gidaspow	EMMS	Filtered	Gidaspow
1	0.94	0.78	0.70	0.68	0.11	0.08	0.12
2	2.04	0.55	0.50	0.49	0.14	0.07	0.07
3	3.09	0.51	0.65	0.40	0.08	0.08	0.09
4	4.13	0.47	0.63	0.69	0.06	0.08	0.05

lower superficial gas velocities, U_g = 0.94 m/s and 2.04 m/s, lateral profiles of the CO_2 concentration ratio predicted by the two-step EMMS/bubbling drag model are in good agreement with the experimental data. MRE of CO_2 concentration ratio at HSV is around 20 % and MAE of CO_2 concentration ratio at LSV is rather smaller (around 0.1), as shown in Table S10 and Table S11 in the Supplementary Materials. At higher superficial gas velocity, U_g = 3.08 m/s and 4.13 m/s, CFD predicted CO_2 concentration ratios are higher than the experimental ones at the left-hand side, i.e., the injection side of simulated volatiles. With increased distance from the injection, CO_2 concentration ratios predicted by CFD decrease more rapidly than the experimental ones and show an increase in the right wall region. The cause for this discrepancy is that the standard k-ε turbulence model can give a good prediction at low turbulent intensity, while a more detailed turbulent model is required for high superficial gas velocity. Another more likely explanation to the discrepancy between CFD simulations and experiments at higher superficial gas velocities is that the measured gas concentrations represent the average concentration at a given position, rather than the average concentration of the entire flow. At higher superficial gas velocities, the fluidization gas from the bottom containing no CO_2 could bypass the bed at a higher velocity. As a results, the suction tube for the gas analyzer may have limited time to collect sufficient gas samples from these bypass flows, potentially leading to higher measured CO_2 concentrations. But both CFD simulations and experiments show that more simulated volatiles can be distributed from the left-hand side to the right side, i.e., the side with injection port, with the help of VD, as compared to the case without VD as shown in Fig. 6.

Fig. 9 compares predicted profiles of axial pressure and CO_2

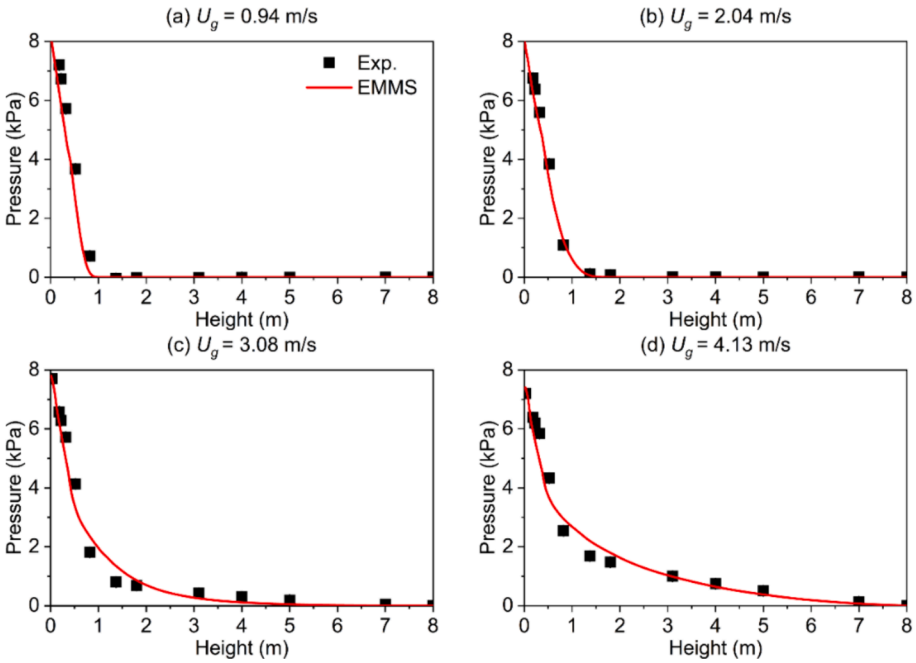

Fig. 7. Comparison of predicted axial pressure profiles of the fluidized bed with VD by the two-step EMMS/bubbling model with experimental data under different superficial gas velocities ((a) U_g = 0.94 m/s, (b) U_g = 2.04 m/s, (c) U_g = 3.09 m/s, (d) U_g = 4.13 m/s).

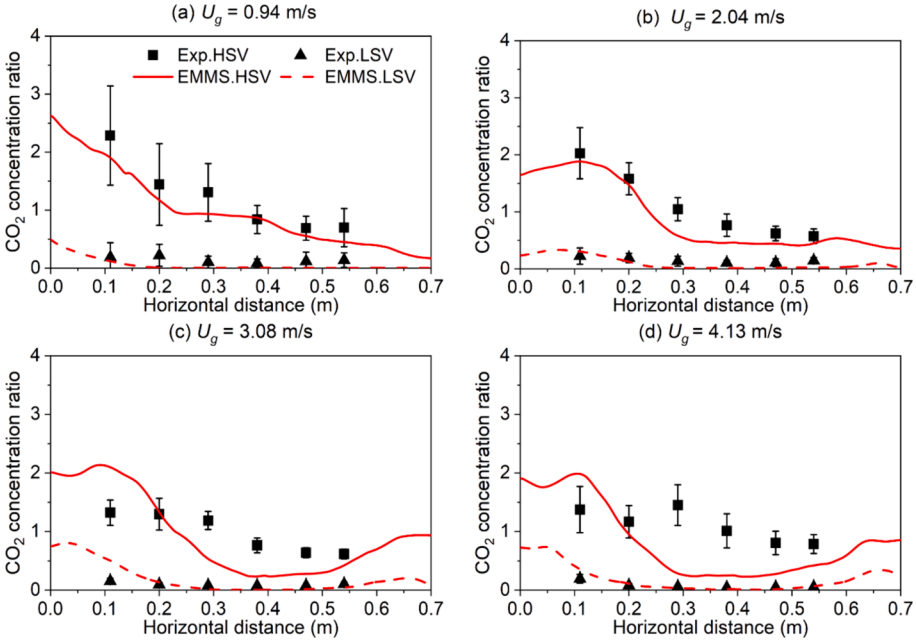

Fig. 8. Comparison of predicted lateral profiles of CO_2 concentration ratio at two different heights of the fluidized bed bottom (HSV: 0.483 m, LSV: 0.138 m) using the two-step EMMS/bubbling model with experimental data under different superficial gas velocity ((a) U_g = 0.94 m/s, V_{SV} = 19 Nm^3/h, (b) U_g = 2.04 m/s, V_{SV} = 65 Nm^3/h, (c) U_g = 3.09 m/s, V_{SV} = 92 Nm^3/h, (d) U_g = 4.13 m/s, V_{SV} = 112 Nm^3/h, while flow rate of simulated volatiles were kept as around 10 % of the primary air) with VD.

concentration by the two-step EMMS/bubbling model with experimental data under varying flow rate of simulated volatiles (V_{SV} is 19, 61, 102 Nm^3/h). Velocity of the primary air is kept constant at 0.94 m/s. The results show that CFD predictions with the two-step EMMS/bubbling model are quantitatively in good agreement with experimental data. This suggests that the two-step EMMS/bubbling mode could give reasonable predictions of hydrodynamic and mass transfer of the experimental setup operated under various conditions, in particular at low superficial gas velocity.

Overall, CFD simulations with the two-step EMMS/bubbling model of the fluidized bed with and without VD are validated with experimental data from two aspects, i.e., profiles of axial pressure and lateral CO_2 concentration ratio. It means the two-step EMMS/bubbling model is suitable to simulate the experimental setup and could give reasonable predictions of hydrodynamic and mass transfer under various operating conditions with or without VD. The results predicted by the two-step EMMS/bubbling model will be further used to evaluate the effects of VD on hydrodynamic behaviors of the fluidized bed.

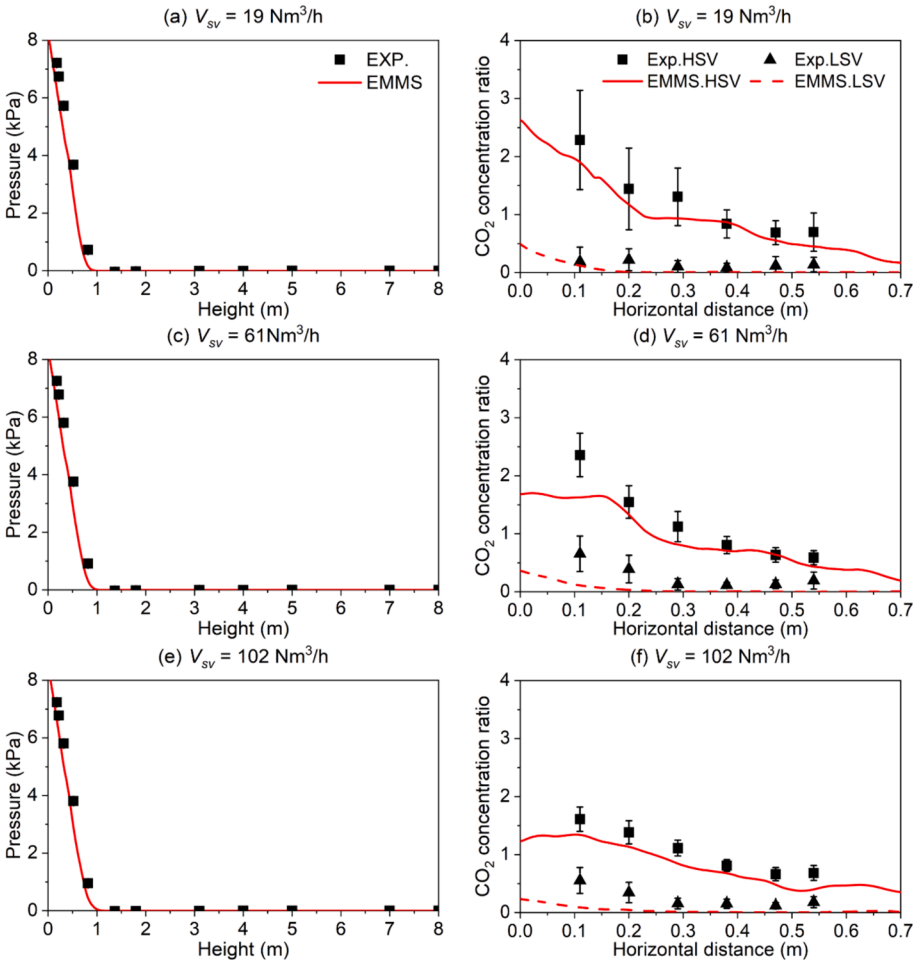

Fig. 9. Comparison of predicted axial pressure profiles ((a), (c), and (e)) and lateral profiles of CO_2 concentration ratio ((b), (d), and (f)) at two different heights (HSV: 0.483 m, LSV: 0.138 m) of the fluidized bed bottom with VD by using the two-step EMMS/bubbling drag model with the experimental data with varying flow rate of the simulated volatile (V_{SV} = 19, 61, 102 Nm^3/h).

4.2. Effects of the VD on hydrodynamics behaviors

4.2.1. Solids volume fraction

Fig. 10 compares instantaneous (a) and time-averaged (b) solids volume fraction of the fluidized bed without (left) and with (right) the VD from the front view under various operating conditions. For the case of U_g = 0.94 m/s, bed expansions without and with the VD are almost the same. A dilute region with low solid concentration near injection port of the simulated volatiles, i.e., the local plume of simulated volatiles, is observed for the case without the VD. When simulated volatiles are injected into the VD, top region of the VD would be free from solid particles due to pressure drop over distribution holes of the VD. When increasing superficial gas velocity to 2.04 m/s and at the same time increasing flow rate of simulated volatiles proportionally, bed materials inside the VD is squeezed outside due to higher pressure drop over the distribution holes, and consequently, bed expansion with the VD is slightly higher than the case without the VD. When superficial gas velocities are 3.09 m/s and 4.13 m/s, upper region of the VD is free from solid particles, similar to the case at U_g = 2.04 m/s. Generally, gas-solids contact time is expected to be increased due to the much more even horizontal distribution and higher vertical bed expansion. Those findings are also consistent with axial pressure profiles of the VD region shown in Fig. S10 in the Supplementary Materials.

To show more details of the effects of the VD on distribution of solids volume fraction at bottom of the fluidized bed, Fig. 11 displays time-averaged solids volume fraction in the YZ plane at X = 0.08 m, 0.35 m, and 0.55 m for the cases without and with the VD. Contour plots of the YZ plane show bottom section of the fluidized bed, i.e., from 0 to 0.6 m high, where the VD has significant effects on primary air flow. For the fluidized bed without the VD, solids volume fraction is relatively constant along the height at bottom section for all operating conditions. However, solids volume fraction decreases from 0.4 to 0.2 with the increase of superficial gas velocity from 0.94 m/s to 4.13 m/s. For the fluidized bed with the VD, solids volume fraction outside the VD is slightly lower than that of the fluidized bed without the VD when height is smaller than 0.4 m, because cross-sectional area for primary air is decreased due to the installation of the VD and the corresponding increase of gas velocity. When height is more than 0.4 m, solids volume fraction increases slightly with increased bed height, as cross-sectional area outside VD gets back to normal cross-section of the fluidized bed. Solids volume fraction inside the VD decreases with height under all investigated operating conditions. But height of the dense phase inside the VD differs among the four different cases, especially when U_g = 0.94 m/s. The contour plots also show that injection of simulated volatiles only has limited effects on distribution of solids volume fraction near the injection port, i.e., X = 0.08 m, in the cases without the VD, while other positions, e.g., 0.35 m and 0.55 m, still maintain the typical 'core-annulus' flow structure in the fluidized bed. Further, part of solids is also recycled back at around 0.4 m to 0.5 m height as cross-sectional area is enlarged, thereby higher solids volume fraction is observed in this region, which is good for mixing between simulated volatiles and solid particles.

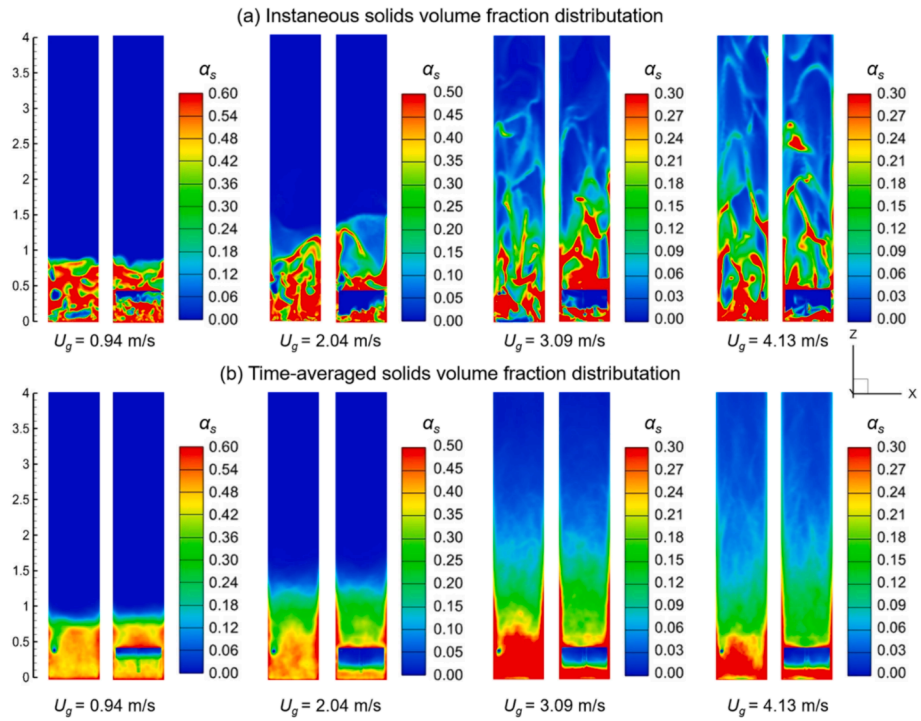

Fig. 10. Instantaneous (a) and time-averaged (b) solids volume fraction of the fluidized bed without (left) and with (right) the VD from the front view under various operating conditions ((a) U_g = 0.94 m/s, (b) U_g = 2.04 m/s, (c) U_g = 3.09 m/s, (d) U_g = 4.13 m/s).

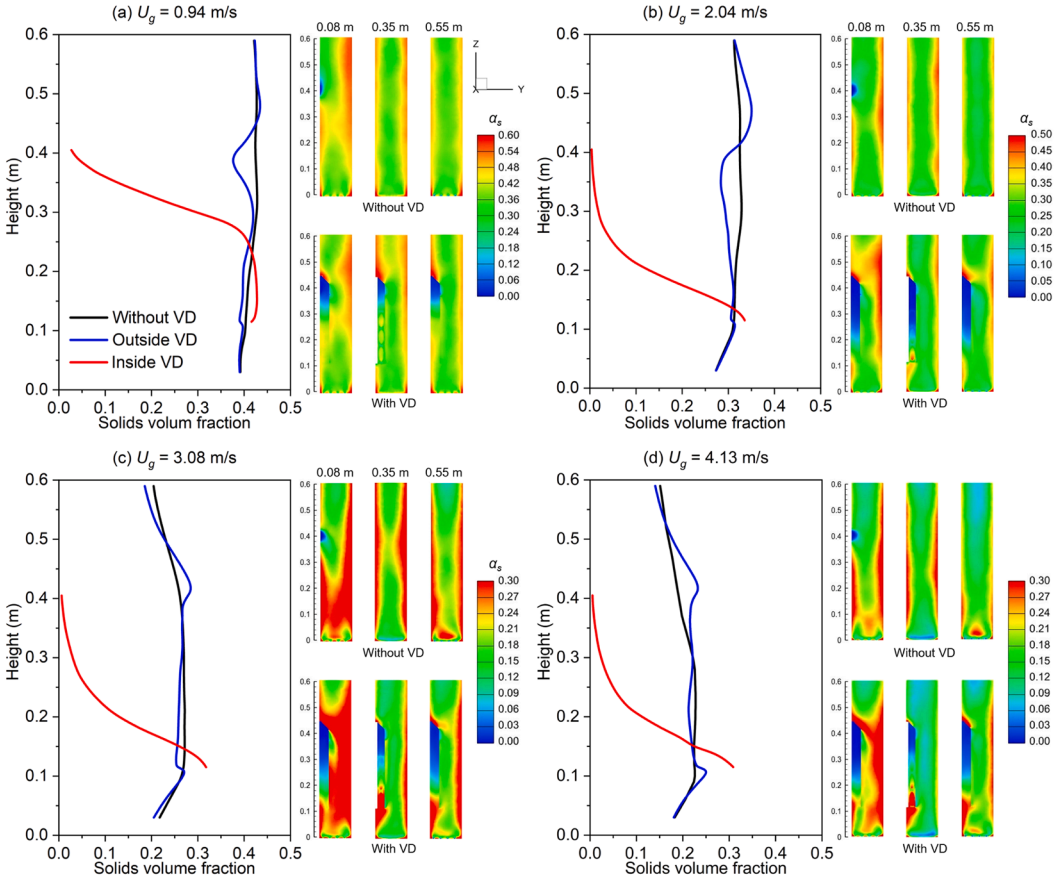

Fig. 11. Axial profiles of time-averaged solids volume fraction along with their contour plots of YZ plane at X = 0.08 m, 0.35 m, and 0.55 m for the cases without and with the VD under various operating conditions ((a) U_g = 0.94 m/s, (b) U_g = 2.04 m/s, (c) U_g = 3.09 m/s, (d) U_g = 4.13 m/s).

4.2.2. Gas flow streamlines

Fig. 12 shows gas velocities and flow streamlines in the YZ plane for the fluidized bed without and with the VD. For the cases without the VD, injection of simulated volatiles only has a significant effect on primary air flow near the injection port of simulated volatiles, i.e., at X = 0.08 m. For the fluidized bed with the VD, the injected simulated volatiles obviously have a certain influence on primary air flow for all selected 2D YZ planes, because simulated volatiles are constrained and laterally distributed by the VD. Thus, the VD is expected to promote mixing and increase contact time between simulated volatiles and solid particles.

Fig. 13 shows gas velocities and flow streamlines in the YZ plane at X = 0.08 m, 0.35 m, and 0.55 m for the fluidized bed with the VD with different flow rates of simulated volatiles and constant primary air flow rate, where V_{air} is set to 234 Nm^3/h. Different flow rates of simulated volatiles could represent different fuel injection rates. As flow of simulated volatiles increases, the effect on primary air flow becomes more significant and flow field forms more vortex-like structures, which might enhance mixing of gas and solids. However, it should also be noted that contact time between solids and volatiles may be decreased, since residence time of volatiles decreases with the increase of its flow rate.

4.2.3. Distribution of CO_2 concentration

As CO_2 is used as tracer gas in the experiments, its distribution can reflect mixing of simulated volatiles with primary air and solid particles. Fig. 14 shows time-averaged CO_2 concentration in the XZ plane (left) and in the XY plane at four heights (right) without and with the VD at different fluidization velocities. For the fluidized bed without the VD, simulated volatiles cannot be well mixed with primary air at bottom section at $U_g = 0.94$ m/s. With increased superficial gas velocity, mixing between simulated volatiles and primary air becomes poorer. But with the VD, simulated volatiles are reasonably well mixed with primary air after distribution of the VD.

To further evaluate the effects of the VD on the mixing between simulated volatiles and primary air at different heights, Fig. 15 shows comparison of lateral profiles of CO_2 concentration ratio at two selected heights, i.e., 0.4 m and 0.8 m, for the fluidized bed without and with the VD under various operating condition. Height of 0.4 m is selected because it is the same as the injection port of simulated volatiles. Height of 0.8 m is selected because this height better reflects the effects of the VD on the horizontal distribution. It is evident that the local plume of simulated volatiles near the injection port is distributed more evenly over the cross-section by the VD. At 0.8 m, CO_2 ratio varies around 1, indicating that simulated volatiles are reasonably well mixed with primary air as well as solid particles. Therefore, the VD is indeed expected to improve combustion efficiency of volatiles in the fluidized-bed system.

5. Conclusion

To have a better understanding of the VD concept and the effects of the VD on hydrodynamic behaviors in order to provide a more solid foundation for future scale-up, a three-dimensional full-loop CFD simulation of the fluidized bed with VD has been conducted. The simulations use an Eulerian multiphase granular model, where a homogenous drag model (the Gidaspow drag model (Gidaspow, 1994)) and two meso-scale drag models, i.e., the filtered drag model (Sarkar et al., 2016) and the two-step EMMS/bubbling drag model (Luo et al., 2017), have been evaluated with experimental data for the fluidized bed without the VD. The results show that all three drag models can generally give reasonable predictions of axial pressure profiles and lateral tracer gas (CO_2) concentration profiles with some deviations, possibly explained by the simplification of gas velocities of primary air inlet in the simulations. However, results from the two-step EMMS/bubbling drag model were closer to experimental results, and selected for further simulations of the fluidized bed with VD. Axial pressure profiles and lateral profile of CO_2 concentration ratio predicted by the two-step EMMS/bubbling drag model are generally in good agreement with experimental data of the fluidized bed with the VD, even though a more detailed turbulent model is required for high superficial gas velocity. The results indicate that the two-step EMMS/bubbling drag model is a suitable drag model in CFD

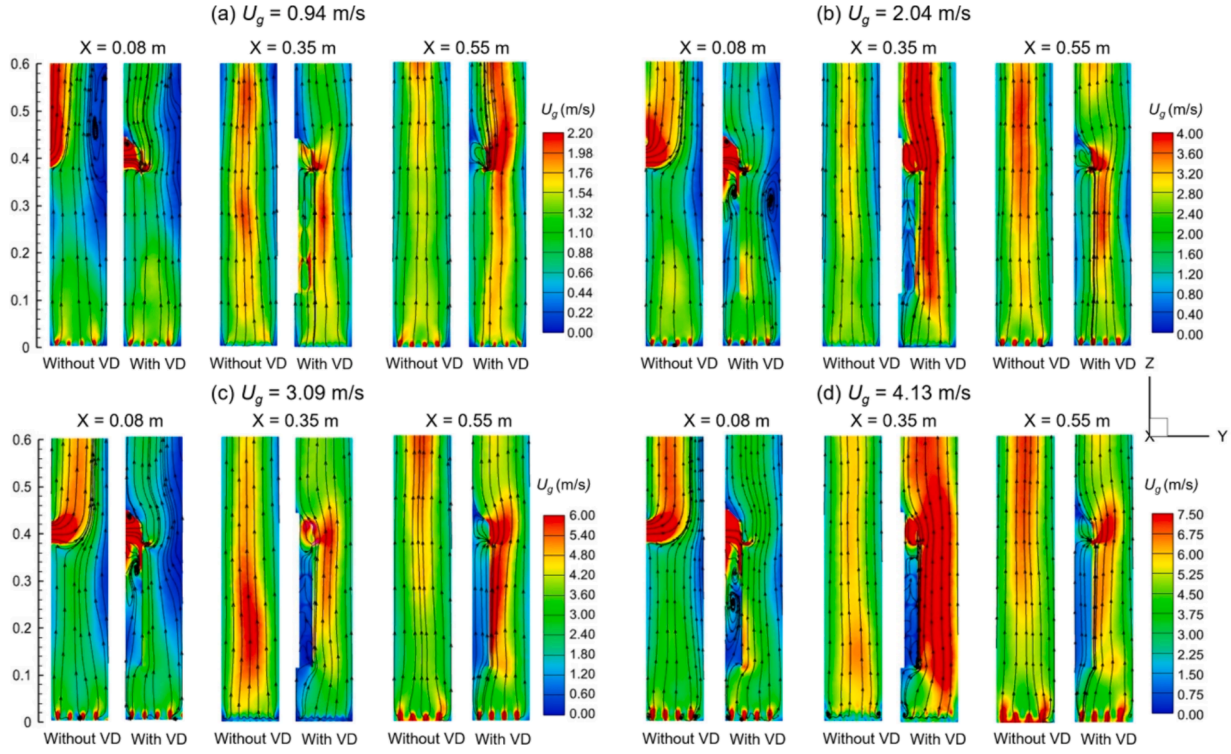

Fig. 12. Comparison of instantaneous gas flow streamlines of the YZ plane of X = 0.08 m, 0.35 m, and 0.55 m for the fluidized bed without and with the VD under various operating conditions ((a) $U_g = 0.94$ m/s, (b) $U_g = 2.04$ m/s, (c) $U_g = 3.09$ m/s, (d) $U_g = 4.13$ m/s).

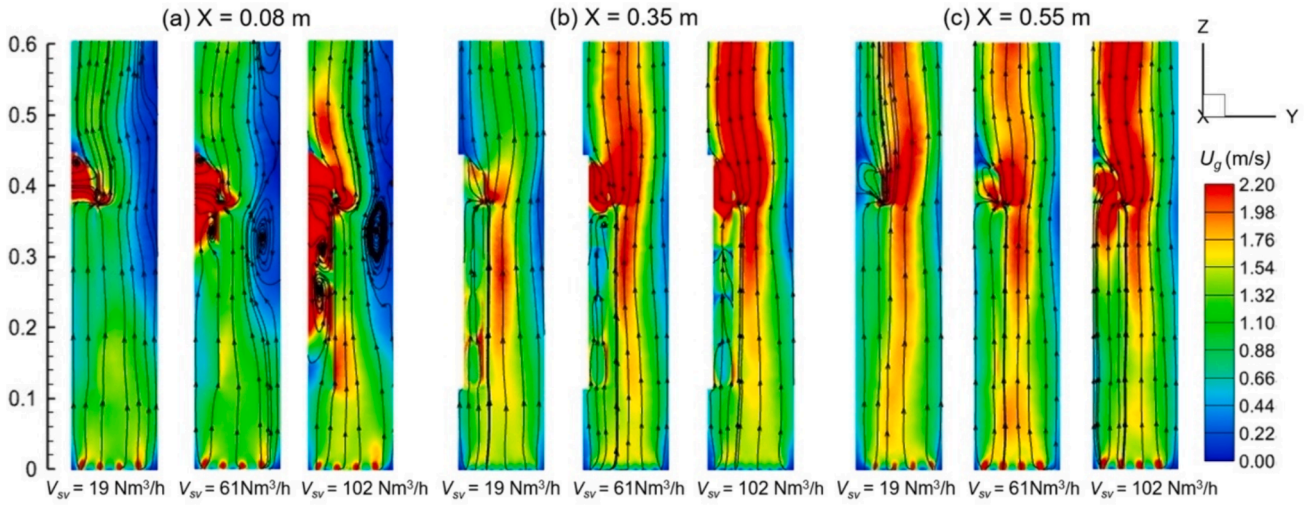

Fig. 13. Instantaneous gas flow streamlines of YZ plane at X = 0.08 m (a), 0.35 m (b), and 0.55 m (c) for the fluidized bed with the VD under different flow rates of simulated volatiles and constant primary air flow rates.

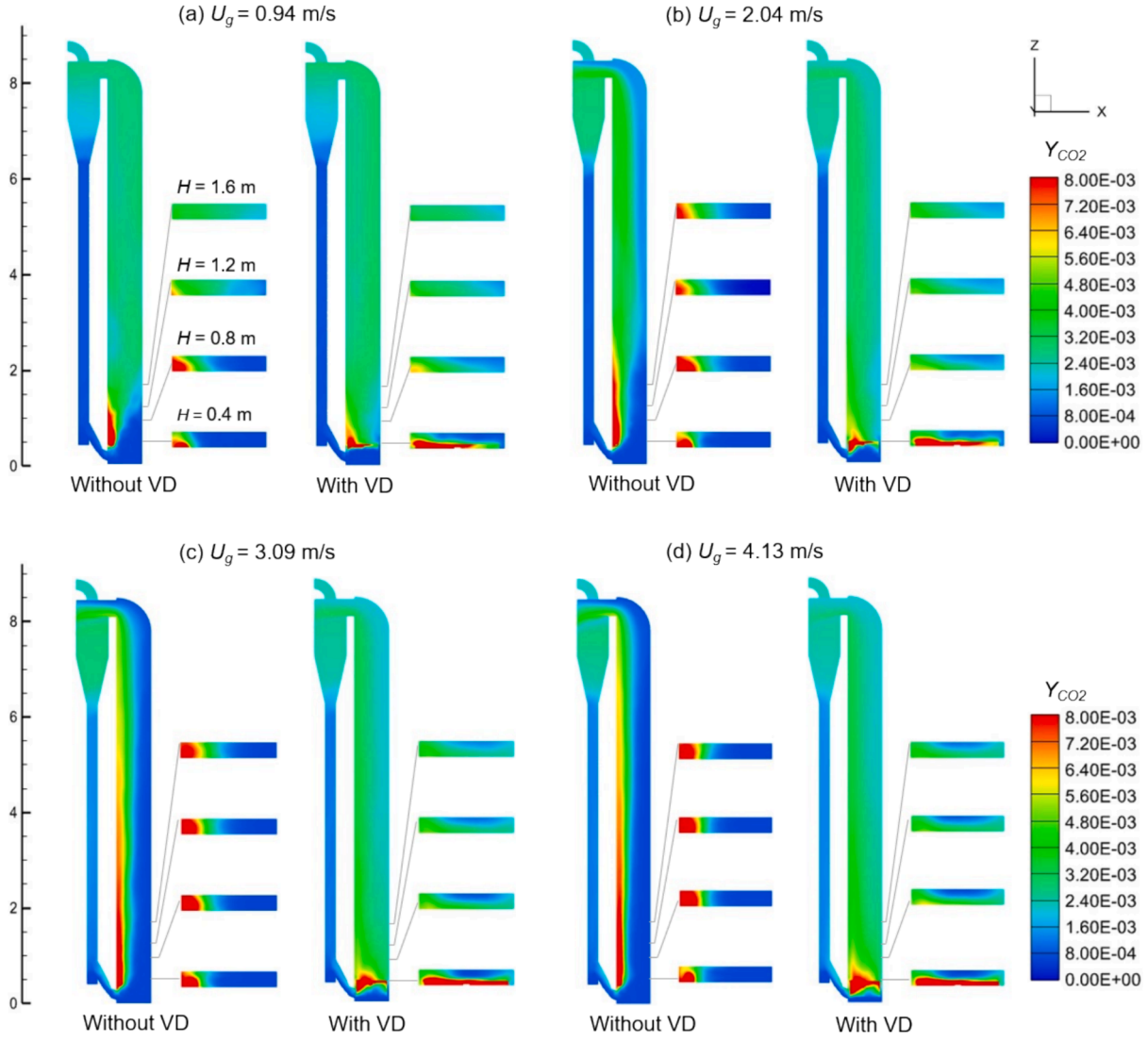

Fig. 14. Comparison of contour plots of time-averaged CO_2 concentration in the fluidized bed without and with the VD under various operating conditions ((a) U_g = 0.94 m/s, (b) U_g = 2.04 m/s, (c) U_g = 3.09 m/s, (d) U_g = 4.13 m/s).

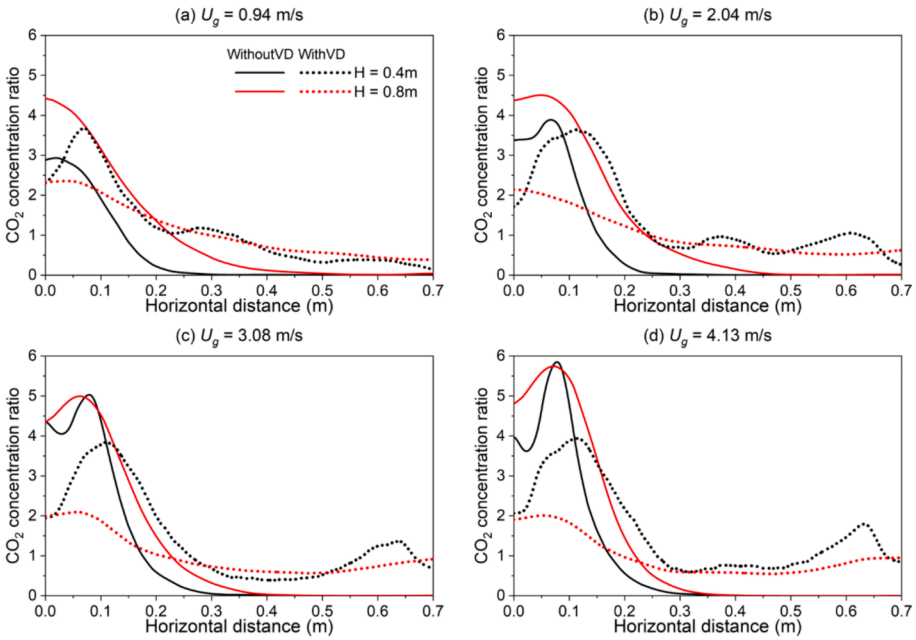

Fig. 15. Comparison of lateral profiles of CO_2 concentration ratio at two selected heights (0.4 m and 0.8 m) for the fluidized bed without and with the VD under various operating conditions ((a) U_g = 0.94 m/s, (b) U_g = 2.04 m/s, (c) U_g = 3.09 m/s, (d) U_g = 4.13 m/s).

modeling of the fluidized bed intensified with the VD under bubbling and turbulent fluidization regime. Three-dimensional analysis of solids volume fraction and gas streamlines of the fluidized bed without and with the VD shows mixing of simulated volatiles with primary air and solid particles is promoted by the VD.

CRediT authorship contribution statement

Xiaobao Wang: Writing – original draft, Software, Methodology, Data curation, Conceptualization. **Xiaoyun Li:** Writing – review & editing, Methodology, Data curation. **Lan Yi:** Methodology. **Anders Lyngfelt:** Supervision, Funding acquisition. **Tobias Mattisson:** Supervision, Funding acquisition. **Xiaoqin Wu:** Visualization. **Hao Luo:** Writing – review & editing, Supervision, Methodology, Funding acquisition. **Qingang Xiong:** Writing – review & editing, Supervision, Funding acquisition.

Declaration of competing interest

The authors declare that they have no known competing financial interests or personal relationships that could have appeared to influence the work reported in this paper.

Data availability

Data will be made available on request.

Acknowledgements

This study was financially supported by the National Natural Science Foundation of China (No. 22208254 and 22178123), the Scientific Research Foundation of Hubei Educational Committee (No. D20221102), and the Swedish Energy Agency (No. 46626-7).

Appendix A. Supplementary data

Supplementary data to this article can be found online at https://doi.org/10.1016/j.ces.2024.120211.

References

Abad, A., Gayán, P., de Diego, L.F., García-Labiano, F., Adánez, J., 2019. Modelling Chemical-Looping assisted by Oxygen Uncoupling (CLaOU): Assessment of natural gas combustion with calcium manganite as oxygen carrier. Proc. Combust. Inst. 37, 4361–4369.
ANSYS, I., 2023. ANSYS Fluent: Theory Guide. Release 2023, R1.
Arjmand, M., Azad, A.-M., Leion, H., Lyngfelt, A., Mattisson, T., 2011. Prospects of Al2O3 and MgAl2O4-Supported CuO Oxygen Carriers in Chemical-Looping Combustion (CLC) and Chemical-Looping with Oxygen Uncoupling (CLOU). Energy Fuel 25, 5493–5502.
Azimi, G., Leion, H., Rydén, M., Mattisson, T., Lyngfelt, A., 2013. Investigation of Different Mn–Fe Oxides as Oxygen Carrier for Chemical-Looping with Oxygen Uncoupling (CLOU). Energy Fuel 27, 367–377.
Benzarti, S., Mhiri, H., Bournot, H., 2021. Numerical simulation of baffled circulating fluidized bed with Geldart B particles. Powder Technol. 380, 629–637.
Berdugo Vilches, T., Lind, F., Rydén, M., Thunman, H., 2017. Experience of more than 1000h of operation with oxygen carriers and solid biomass at large scale. Appl. Energy 190, 1174–1183.
Daneshmand-Jahromi, S., Sedghkerdar, M.H., Mahinpey, N., 2023. A review of chemical looping combustion technology: Fundamentals, and development of natural, industrial waste, and synthetic oxygen carriers. Fuel 341.
Ding, K., Xiong, Q., Zhong, Z., Zhong, D., Zhang, Y., 2020. CFD simulation of combustible solid waste pyrolysis in a fluidized bed reactor. Powder Technol. 362, 177–187.
Du, C., Han, C., Yang, Z., Wu, H., Luo, H., Niedzwiecki, L., Lu, B., Wang, W., 2022. Multiscale CFD Simulation of an Industrial Diameter-Transformed Fluidized Bed Reactor with Artificial Neural Network Analysis of EMMS Drag Markers. Ind. Eng. Chem. Res.
Ergun, S., 1952. Fluid Flow through Packed Columns. Chem. Eng. Prog 48, 89–94.
Gayán, P., Adánez-Rubio, I., Abad, A., de Diego, L.F., García-Labiano, F., Adánez, J., 2012. Development of Cu-based oxygen carriers for Chemical-Looping with Oxygen Uncoupling (CLOU) process. Fuel 96, 226–238.
Geldart, D., 1973. Types of gas fluidization. Powder Technol. 7, 285–292.
Gidaspow, D., Bezburuah, R., Ding, J., 1991. Hydrodynamics of circulating fluidized beds: kinetic theory approach. Illinois Inst. of Tech., Chicago, IL (United States). Dept. of Chemical ….
Gidaspow, D., 1994. Multiphase Flow and Fluidization.
Guío-Pérez, D.C., Pröll, T., Hofbauer, H., 2014. Influence of ring-type internals on the solids residence time distribution in the fuel reactor of a dual circulating fluidized bed system for chemical looping combustion. Chem. Eng. Res. Des. 92, 1107–1118.
Hedayati, A., Soleimanisalim, A.H., Mattisson, T., Lyngfelt, A., 2022. Thermochemical conversion of biomass volatiles via chemical looping: Comparison of ilmenite and steel converter waste materials as oxygen carriers. Fuel 313, 122638.
Igci, Y., Andrews, A.T., Sundaresan, S., Pannala, S., O'Brien, T., 2008. Filtered two-fluid models for fluidized gas-particle suspensions. AIChE J 54, 1431–1448.
Igci, Y., Pannala, S., Benyahia, S., Sundaresan, S., 2011. Validation Studies on Filtered Model Equations for Gas-Particle Flows in Risers. Ind. Eng. Chem. Res. 51, 2094–2103.
Karlsson, T., Liu, X., Pallarès, D., Johnsson, F., 2017. Solids circulation in circulating fluidized beds with low riser aspect ratio and varying total solids inventory. Powder Technol. 316, 670–676.

Krzywanski, J., Sztekler, K., Szubel, M., Siwek, T., Nowak, W., Mika, Ł., 2020a. A Comprehensive Three-Dimensional Analysis of a Large-Scale Multi-Fuel CFB Boiler Burning Coal and Syngas. Part 1. The CFD Model of a Large-Scale Multi-Fuel CFB Combustion. Entropy 22, 964.

Krzywanski, J., Sztekler, K., Szubel, M., Siwek, T., Nowak, W., Mika, Ł., 2020b. A Comprehensive, Three-Dimensional Analysis of a Large-Scale, Multi-Fuel, CFB Boiler Burning Coal and Syngas. Part 2. Numerical Simulations of Coal and Syngas Co-Combustion. Entropy 22, 856.

Krzywanski, J., Czakiert, T., Zylka, A., Nowak, W., Sosnowski, M., Grabowska, K., Skrobek, D., Sztekler, K., Kulakowska, A., Ashraf, W.M., Gao, Y., 2022. Modelling of SO2 and NOx Emissions from Coal and Biomass Combustion in Air-Firing, Oxyfuel, iG-CLC, and CLOU Conditions by Fuzzy Logic Approach. Energies 15, 8095.

Larring, Y., Pishahang, M., Tolchard, J., Lind, A.M., Sunding, M.F., Stensrød, R.E., Jacobs, M., Snijkers, F., van der Kolk, T., Albertsen, K., 2020. Fabrication process parameters significantly affect the perovskite oxygen carriers materials (OCM) performance in chemical looping with oxygen uncoupling (CLOU). J. Therm. Anal. Calorim. 140, 577–589.

Li, T., Dietiker, J.-F., Shadle, L., 2014. Comparison of full-loop and riser-only simulations for a pilot-scale circulating fluidized bed riser. Chem. Eng. Sci. 120, 10–21.

Li, J., Huang, W., 2018. From Multiscale to Mesoscience: Addressing Mesoscales in Mesoregimes of Different Levels. Annu Rev Chem Biomol Eng 9, 41–60.

Li, X., Lyngfelt, A., Mattisson, T., 2021. An experimental study of a volatiles distributor for solid fuels chemical-looping combustion process. Fuel Process. Technol. 220, 106898.

Li, X., Lyngfelt, A., Linderholm, C., Leckner, B., Mattisson, T., 2022a. Performance of a volatiles distributor equipped with internal baffles under different fluidization regimes. Powder Technol. 409, 117807.

Li, X., Lyngfelt, A., Pallarès, D., Linderholm, C., Mattisson, T., 2022b. Investigation on the Performance of Volatile Distributors with Different Configurations under Different Fluidization Regimes. Energy Fuel 36, 9571–9587.

Linderholm, C., Lyngfelt, A., Cuadrat, A., Jerndal, E., 2012. Chemical-looping combustion of solid fuels – Operation in a 10kW unit with two fuels, above-bed and in-bed fuel feed and two oxygen carriers, manganese ore and ilmenite. Fuel 102, 808–822.

Liu, L., Li, Z., Wang, Y., Li, Z., Larring, Y., Cai, N., 2022. Industry-scale production of a perovskite oxide as oxygen carrier material in chemical looping. Chem. Eng. J. 431, 134006.

Lu, B., Zhang, N., Wang, W., Li, J., Chiu, J.H., Kang, S.G., 2013. 3-D full-loop simulation of an industrial-scale circulating fluidized-bed boiler. AIChE J. 59, 1108–1117.

Lu, L., Xu, J., Ge, W., Gao, G., Jiang, Y., Zhao, M., Liu, X., Li, J., 2016. Computer virtual experiment on fluidized beds using a coarse-grained discrete particle method—EMMS-DPM. Chem. Eng. Sci. 155, 314–337.

Luo, H., Lu, B., Zhang, J., Wu, H., Wang, W., 2017. A grid-independent EMMS/bubbling drag model for bubbling and turbulent fluidization. Chem. Eng. J. 326, 47–57.

Luo, H., Lin, W., Song, W., Li, S., Dam-Johansen, K., Wu, H., 2019. Three dimensional full-loop CFD simulation of hydrodynamics in a pilot-scale dual fluidized bed system for biomass gasification. Fuel Process. Technol. 195, 106146.

Luo, H., Wang, X., Liu, X., Wu, X., Shi, X., Xiong, Q., 2022. A review on CFD simulation of biomass pyrolysis in fluidized bed reactors with emphasis on particle-scale models. J. Anal. Appl. Pyrol. 162, 105433.

Lyngfelt, A., mand, L.-E., Leckner, B., 1996. Progress of combustion in the furnace of a circulating fluidized bed boiler. Symp. (Int.) Combust. 26, 3253–3259.

Lyngfelt, A., Moldenhauer, P., Biermann, M., Johannsen, K., Wimmer, D., Hanning, M., 2023. Operational experiences of chemical-looping combustion with 18 manganese ores in a 300W unit. Int. J. Greenhouse Gas Control 127, 103937.

Masson-Delmotte, V., Zhai, P., Pirani, A., Connors, S.L., Péan, C., Berger, S., Caud, N., Chen, Y., Goldfarb, L., Gomis, M.I., Huang, M., Leitzell, K., Lonnoy, E., Matthews, J. B.R., Maycock, T.K., Waterfield, T., Yelekçi, O., Yu, R., (Eds.), B.Z., 2021. IPCC, 2021: Summary for Policymakers. In: Climate Change 2021: The Physical Science Basis. Contribution of Working Group I to the Sixth Assessment Report of the Intergovernmental Panel on Climate Change, In Press ed.

Milioli, C.C., Milioli, F.E., 2023. A scale sensitive filtered sub-grid drag model for fluidized gas-particle flows. Chem. Eng. Sci. 267, 118266.

Moldenhauer, P., Hallberg, P., Biermann, M., Snijkers, F., Albertsen, K., Mattisson, T., Lyngfelt, A., 2020. Oxygen-Carrier Development of Calcium Manganite-Based Materials with Perovskite Structure for Chemical-Looping Combustion of Methane. Energ. Technol. 8, 2000069.

Ozarkar, S.S., Yan, X., Wang, S., Milioli, C.C., Milioli, F.E., Sundaresan, S., 2015. Validation of filtered two-fluid models for gas–particle flows against experimental data from bubbling fluidized bed. Powder Technol. 284, 159–169.

Pérez-Vega, R., Abad, A., Bueno, J.A., García-Labiano, F., Gayán, P., de Diego, L.F., Adánez, J., 2019. Improving the efficiency of Chemical Looping Combustion with coal by using ring-type internals in the fuel reactor. Fuel 250, 8–16.

Qasim, M., Ayoub, M., Aqsha, A., Ghazali, N.A., Ullah, S., Ando, Y., Farrukh, S., 2022. Investigation on the Redox Properties of a Novel Cu-Based Pr-Modified Oxygen Carrier for Chemical Looping Combustion. ACS Omega 7, 40789–40798.

Rydén, M., Johansson, M., Cleverstam, E., Lyngfelt, A., Mattisson, T., 2010. Ilmenite with addition of NiO as oxygen carrier for chemical-looping combustion. Fuel 89, 3523–3533.

Samruamphianskun, T., Piumsomboon, P., Chalermsinsuwan, B., 2012. Effect of ring baffle configurations in a circulating fluidized bed riser using CFD simulation and experimental design analysis. Chem. Eng. J. 210, 237–251.

Sarkar, A., Milioli, F.E., Ozarkar, S., Li, T., Sun, X., Sundaresan, S., 2016. Filtered sub-grid constitutive models for fluidized gas-particle flows constructed from 3-D simulations. Chem. Eng. Sci. 152, 443–456.

Shao, Y., Agarwal, R.K., Wang, X., Jin, B., 2020. Numerical simulation of a 3D full loop iG-CLC system including a two-stage counter-flow moving bed air reactor. Chem. Eng. Sci. 217.

Shi, Z., Wang, W., Li, J., 2011. A bubble-based EMMS model for gas–solid bubbling fluidization. Chem. Eng. Sci. 66, 5541–5555.

Shulman, A., Cleverstam, E., Mattisson, T., Lyngfelt, A., 2009. Manganese/Iron, Manganese/Nickel, and Manganese/Silicon Oxides Used in Chemical-Looping With Oxygen Uncoupling (CLOU) for Combustion of Methane. Energy Fuel 23, 5269–5275.

Skulimowska, A., Di Felice, L., Kamińska-Pietrzak, N., Celińska, A., Pławecka, M., Hercog, J., Krauz, M., Aranda, A., 2017. Chemical looping with oxygen uncoupling (CLOU) and chemical looping combustion (CLC) using copper-enriched oxygen carriers supported on fly ash. Fuel Process. Technol. 168, 123–130.

Stamatopoulos, P., Stefanitsis, D., Zeneli, M., Nikolopoulos, N., 2023. Development of an artificial neural network EMMS drag model for the simulation of fluidized beds in chemical looping combustion. Chem. Eng. Sci. 282, 119286.

Sundaresan, S., Ozel, A., Kolehmainen, J., 2018. Toward Constitutive Models for Momentum, Species, and Energy Transport in Gas-Particle Flows. Annu Rev Chem Biomol Eng 9, 61–81.

Tu, Q., Wang, H., Ocone, R., 2022. Application of three-dimensional full-loop CFD simulation in circulating fluidized bed combustion reactors – A review. Powder Technol. 399, 117181.

Wang, W., Li, J., 2007. Simulation of gas–solid two-phase flow by a multi-scale CFD approach—of the EMMS model to the sub-grid level. Chem. Eng. Sci. 62, 208–231.

Wen, C.Y., 1966. Mechanics of Fluidization. Chem. Eng. Prog., Symp. Ser 62.

Yan, J., Zhang, L., He, J., Liu, M., Lei, Z., Li, Z., Wang, Z., Ren, S., Shui, H., 2022. Boosting chemical looping combustion performances of red mud with transition metal oxides. Carbon Resources Conversion 5, 119–130.

Zhang, Y., Chao, Z., Jakobsen, H.A., 2017. Modelling and simulation of chemical looping combustion process in a double loop circulating fluidized bed reactor. Chem. Eng. J. 320, 271–282.

Zhu, L.-T., Liu, Y.-X., Tang, J.-X., Luo, Z.-H., 2019. A material-property-dependent sub-grid drag model for coarse-grained simulation of 3D large-scale CFB risers. Chem. Eng. Sci. 204, 228–245.

Zylka, A., Krzywanski, J., Czakiert, T., Idziak, K., Sosnowski, M., de Souza-Santos, M.L., Sztekler, K., Nowak, W., 2020. Modeling of the Chemical Looping Combustion of Hard Coal and Biomass Using Ilmenite as the Oxygen Carrier. Energies 13, 5394.

Appendix A. Supplementary data

CFD modeling of a fluidized bed with volatiles distributor for biomass chemical looping combustion

Xiaobao Wang[a,#], Xiaoyun Li[b,#], Lan Yi[a], Anders Lyngfelt[b], Tobias Mattisson[b], Xiaoqin Wu[a], Hao Luo[a,], Qingang Xiong[c,*]*

[a]*School of Chemistry and Chemical Engineering, Hubei Key Laboratory of Coal Conversion and New Carbon Materials, Wuhan University of Science and Technology, Wuhan, 430081, China*

[b]*Division of Energy Technology, Department of Space, Earth and Environment, Chalmers University of Technology, 412 96 Gothenburg, Sweden*

[c]*State Key Laboratory of Pulp and Paper Engineering, South China University of Technology, Guangzhou, 510640, China*

[#] *These authors contributed equally to this work.*

**Corresponding author. Email: haoluo@wust.edu.cn (H. Luo), qingangxiong@scut.edu.cn (Q. Xiong)*

1. Physical properties of the gas species

Table S1 gives the detailed viscosity and density data for different gases (N_2, O_2, and CO_2) under experimental conditions. Cases 1-4 represent the experimental condition without the novel VD, while cases 5-10 represent the experimental condition with the novel VD.

Table S1. Physical properties of N_2, O_2, and CO_2.

Case	ρ_{N2} kg/m³	ρ_{O2} kg/m³	ρ_{CO2} kg/m³	μ_{N2} (Pa·s)·10⁵	μ_{O2} (Pa·s)·10⁵	μ_{CO2} (Pa·s)·10⁵
Experiments without the novel VD						
1	1.123	1.283	1.764	1.798	2.094	1.525
2	1.090	1.245	1.712	1.839	2.145	1.568
3	1.085	1.240	1.705	1.845	2.153	1.575
4	1.082	1.237	1.701	1.849	2.157	1.578
Experiments with the novel VD						
5	1.118	1.277	1.756	1.804	2.102	1.531
6	1.101	1.258	1.730	1.825	2.128	1.553
7	1.093	1.249	1.717	1.835	2.140	1.564
8	1.097	1.253	1.723	1.830	2.134	1.559
9	1.085	1.240	1.704	1.846	2.153	1.575
10	1.081	1.235	1.698	1.851	2.160	1.581

Densities of different gas species of different temperature conditions are determined by using the ideal gas law as given in Eq. (S1).

$$\rho = \frac{PM}{RT} \tag{S1}$$

Here, P is pressure, Pa, M is the molar mass of the gas species, kg/mol, R is gas constant R = 8.314 J/(mol·K), and T is temperature, K. Viscosities of N_2, O_2, and CO_2 are determined by Eqs. (S2)-(S4). These correlations of viscosity can be found in the DIPPR database (https://dippr.aiche.org/).

$$\mu_{N_2} = \frac{1.101\times10^{-7}T^{0.6081}}{1.0+54.714/T} \tag{S2}$$

$$\mu_{O_2} = \frac{1.101\times10^{-6}T^{0.5634}}{1.0+96.3/T} \tag{S3}$$

$$\mu_{CO_2} = \frac{2.148\times10^{-6}T^{0.46}}{1.0+290.0/T} \tag{S4}$$

2. The governing equations of Eulerian multi-phase granular model

Table S2. Eulerian multi-phase granular model.

Governing equations
Continuity equations:
$\frac{\partial}{\partial t}\left(\alpha_g \rho_g\right)+\nabla \cdot\left(\alpha_g \rho_g \boldsymbol{u}_g\right)=0$
$\frac{\partial}{\partial t}\left(\alpha_s \rho_s\right)+\nabla \cdot\left(\alpha_s \rho_s \boldsymbol{u}_s\right)=0$
Momentum equations：
$\frac{\partial}{\partial t}\left(\alpha_g \rho_g \boldsymbol{u}_g\right)+\nabla \cdot\left(\alpha_g \rho_g \boldsymbol{u}_g \boldsymbol{u}_g\right)=-\alpha_g \nabla \boldsymbol{p}_g+\nabla \cdot \boldsymbol{\tau}_g+\alpha_g \rho_g \boldsymbol{g}+\beta\left(\boldsymbol{u}_s-\boldsymbol{u}_g\right)$
$\frac{\partial}{\partial t}\left(\alpha_s \rho_s \boldsymbol{u}_s\right)+\nabla \cdot\left(\alpha_s \rho_s \boldsymbol{u}_s \boldsymbol{u}_s\right)=-\alpha_s \nabla \boldsymbol{p}_s+\nabla \cdot \boldsymbol{\tau}_s+\alpha_s \rho_s \boldsymbol{g}+\beta\left(\boldsymbol{u}_g-\boldsymbol{u}_s\right)$
Gas and solid stress tensors：
$\boldsymbol{\tau}_g=\alpha_g \mu_g\left[\nabla \boldsymbol{u}_g+\left(\nabla \boldsymbol{u}_g\right)^T\right]-\frac{2}{3} \alpha_g \mu_g \nabla \cdot \boldsymbol{u}_g \boldsymbol{I}$
$\boldsymbol{\tau}_s=\alpha_s \mu_s\left(\nabla \boldsymbol{u}_s+\nabla \boldsymbol{u}_s^T\right)+\alpha_s\left(\lambda_s-\frac{2}{3} \mu_s\right) \nabla \cdot \boldsymbol{u}_s \boldsymbol{I}$
Species Transport Equations：
$\frac{\partial\left(\alpha_g \rho_g Y_{g,i}\right)}{\partial t}+\nabla \cdot\left(\alpha_g \rho_g \boldsymbol{u}_g Y_{g,i}\right)=-\nabla \cdot\left(\alpha_g \boldsymbol{J}_{g,i}\right)$
Where: $\boldsymbol{J}_{g,i}=-\left(\rho_g D_{i,m}+\frac{\mu_t}{\mathrm{Sc}_t}\right) \nabla Y_{g,i}$
The standard k-ε turbulence model:
$\frac{\partial}{\partial t}\left(\rho_g \alpha_g k\right)+\nabla \cdot\left(\rho_g \alpha_g \boldsymbol{u}_g k\right)=\nabla \cdot\left[\alpha_g\left(\mu_g+\frac{\mu_t}{\sigma_k}\right) \nabla k\right]+\alpha_g G_k-\rho_g \alpha_g \varepsilon$
$\frac{\partial}{\partial t}\left(\rho_g \alpha_g \varepsilon\right)+\nabla \cdot\left(\rho_g \alpha_g \boldsymbol{u}_g \varepsilon\right)=\nabla \cdot\left[\alpha_g\left(\mu_g+\frac{\mu_t}{\sigma_\varepsilon}\right) \nabla \varepsilon\right)+\alpha_g \frac{\varepsilon}{k}\left[C_1 G_k-C_2 \rho_g \varepsilon\right]$
Where: $C_\mu=0.09, C_1=1.44, C_2=1.92, \sigma_k=1.0, \sigma_\varepsilon=1.3$

Table S3. Constitutive models of the solids phase for different drag models.

KTGF Based drag model (Gidaspow and two-step EMMS/bubbling drag model)	Filtered drag model (ANSYS, 2023)
Solids shear viscosity: $\mu_s = \mu_{s,col} + \mu_{s,kin} + \mu_{s,fr}$	$\mu_s = \rho_s \left(\frac{\boldsymbol{g}}{u_t^2}\right)^{-6/7} \Delta_{filter}^{8/7} S_s \frac{0.00307\alpha_s^{1.544}}{\alpha_{s,\max} - \alpha_s}$
Collisional Viscosity:	where: $\Delta_{filter} = 2V_{cell}^{1/3}$
$\mu_{s,col} = \frac{4}{5}\alpha_s \rho_s d_s g_0 (1+e_s)\left(\frac{\Theta_s}{\pi}\right)^{1/2}$	
Kinetic Viscosity: $\mu_{s,kin} = \frac{10\rho_s d_s \sqrt{\Theta_s \pi}}{96\alpha_s (1+e_s) g_0}\left[1+\frac{4}{5}g_0\alpha_s(1+e_s)\right]^2$	
Frictional viscosity: $\mu_{s,fr} = \frac{p_{friction}\sin\varphi}{2\sqrt{\boldsymbol{I}_{2D}}}$	
Granular bulk viscosity: $\lambda_s = \frac{4}{3}\alpha_s^2 \rho_s d_s g_0 (1+e_s)\left(\frac{\Theta_s}{\pi}\right)^{1/2}$	0
Granular temperature: $\left(-p_s\boldsymbol{I} + \boldsymbol{\tau}_s\right):\nabla \boldsymbol{u}_s - \gamma_{\theta_s} + \varphi_{gs} = 0$	0
Solids pressure: $p_s = \alpha_s\rho_s\Theta_s + 2\rho_s(1+e_s)\alpha_s^2 g_0 \Theta_s$	$p_s = \rho_s \Delta_{filter}^2 S_s^2 \left(0.019\left(\Delta_{filter}^*\right)^2 + 0.006\Delta_{filter}^* + 0.046\right)\alpha_s^{\left(0.27\Delta_{filter}^* + 0.9\right)}$ where: $\Delta_{filter}^* = \frac{\Delta_{filter}\boldsymbol{g}}{u_t^2}$
Radial distribution: $g_0 = \left[1 - \left(\frac{\alpha_s}{\alpha_{s,\max}}\right)^{\frac{1}{3}}\right]^{-1}$	0

3. Geometry and computational domain discretization of the fluidized bed

Geometry model of the cold-flow experimental setup was established by ANSYS SpaceClaim 2023 R1. Then the geometry model was imported to the Meshing module of ANSYS Fluent 2023 R1 to discretize the computational domain. The details on global grid settings are given in Table S4. A gird encryption processing was applied to the grid at bottom of the fluidized bed (0-0.6m) to ensure that the injection port of simulated volatiles, primary

air inlet, and distribution holes of VD have at least 15 points, as performance of the VD in the dense bed is focused. This approach is crucial for optimizing simulation computations, as it enhances computational efficiency while ensuring model accuracy (Krzywanski et al., 2020a, b). Detailed view of the mesh for the fluidized bed with and without VD is given in Fig. S1.

Table S4. Global settings to discretize the computational domain.

Defaults	
Workflow	Watertight Geometry
Physics Preference	CFD
Solver Preference	Fluent
Surface Mesh	
Minimum face Size	1.5 mm
Maximum face Size	25 mm
Groth Rate	1.2
Size Function	Proximity and Curvature
Curvature Normal Angle	Default (18.0°)
Cells Per Gap	1
Scope Proximity To	edges
Add Boundary Layers	None
Volume Mesh	
Filled With	polyhrdra
Sizing Method	Global
Max Cell Length	25 mm

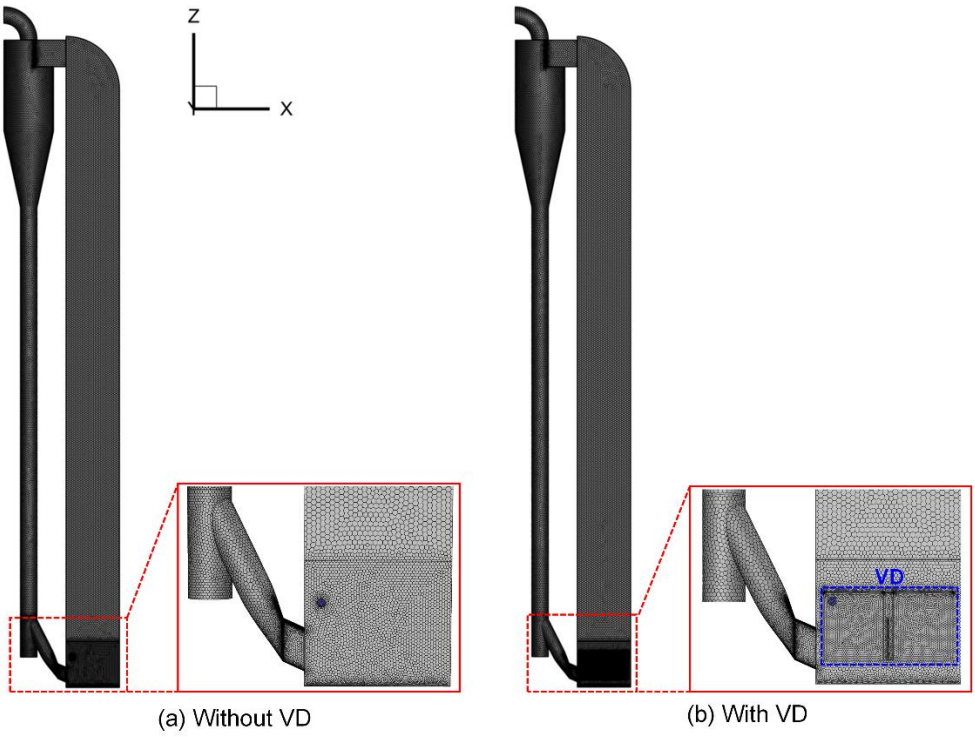

Fig. S1. Detailed view of the mesh for the fluidized bed without VD (a) and with VD (b).

The primary air distributor is streamlined to 184 holes with diameter of 6 mm, maintaining the same opening ratio as the original 1660 holes with diameter of 2 mm. This simplification reduces the total mesh number from 4 million to approximately 412 and 560 thousand polyhedral meshes for the cases with VD and without VD, resulting in a significant reduction in computational time. The corresponding average mesh size is about 61 and 55 times of the particle diameter, which is acceptable for E-E modeling (Luo et al., 2017). To evaluate quality of the mesh, a study was conducted focusing primarily on skewness and orthogonal quality. As given in Table S5, maximum skewness is 0.864 and 0.636 and minimum orthogonal quality is 0.301 and 0.300 for the case without VD and with VD, respectively. Thus, maximum skewness is smaller than 0.95 and minimum orthogonal quality is larger than 0.05, indicating that the grid is fine enough for CFD modeling (Krzywanski et al., 2020a, b).

Table S5. Selected parameters of the analyzed grid quality indicators.

Items	Without VD	With VD
Maximum skewness	0.864	0.636
Minimum orthogonal quality	0.301	0.300

The number of cells distributed in the generated grid according to skewness of the cases without and with VD is illustrated in Fig. S2 and Fig. S3. Skewness of most of the cells is in the range of 0.0-0.3. The number of cells distributed in the generated grid according to orthogonal quality of the cases without and with VD is given in Fig. S4 and Fig. S5. Orthogonal quality of most of the cells is in the range of 0.7-1.0. These results also indicate that quality of the grid satisfies the requirements of CFD modeling.

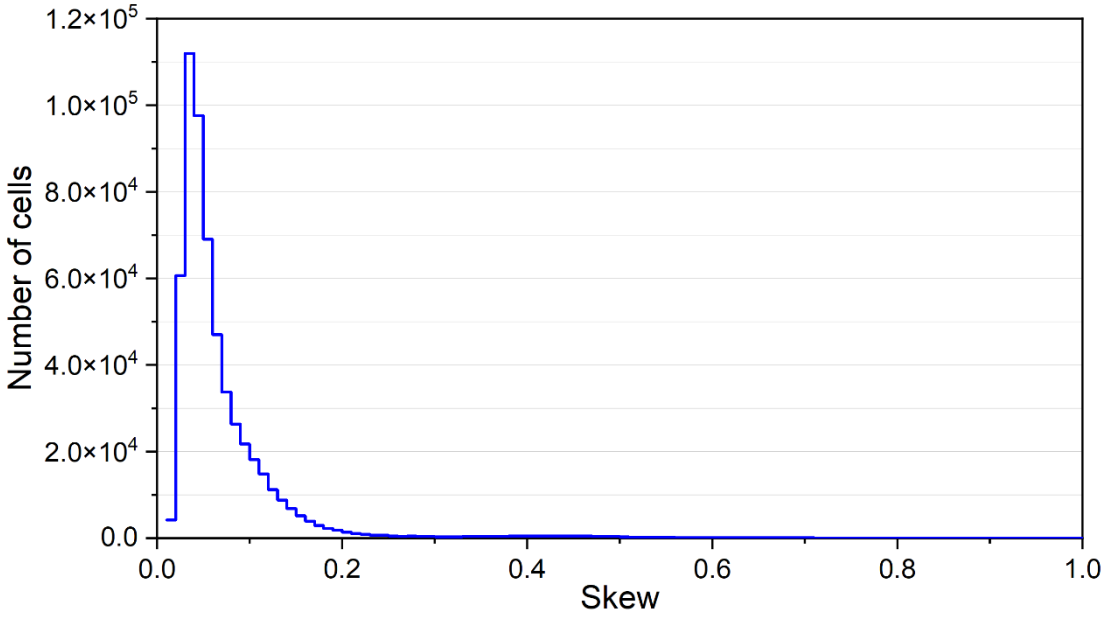

Fig. S2. Mesh elements distribution for the model without VD installation generated based on skew.

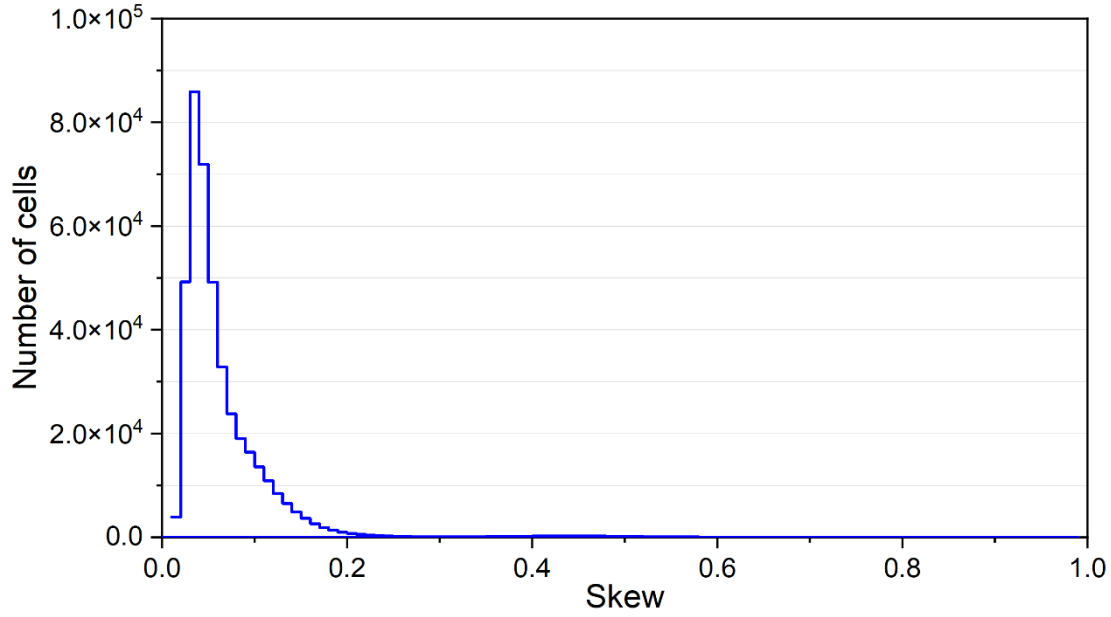

Fig. S3. Mesh elements distribution for the model with VD installation generated based on skew.

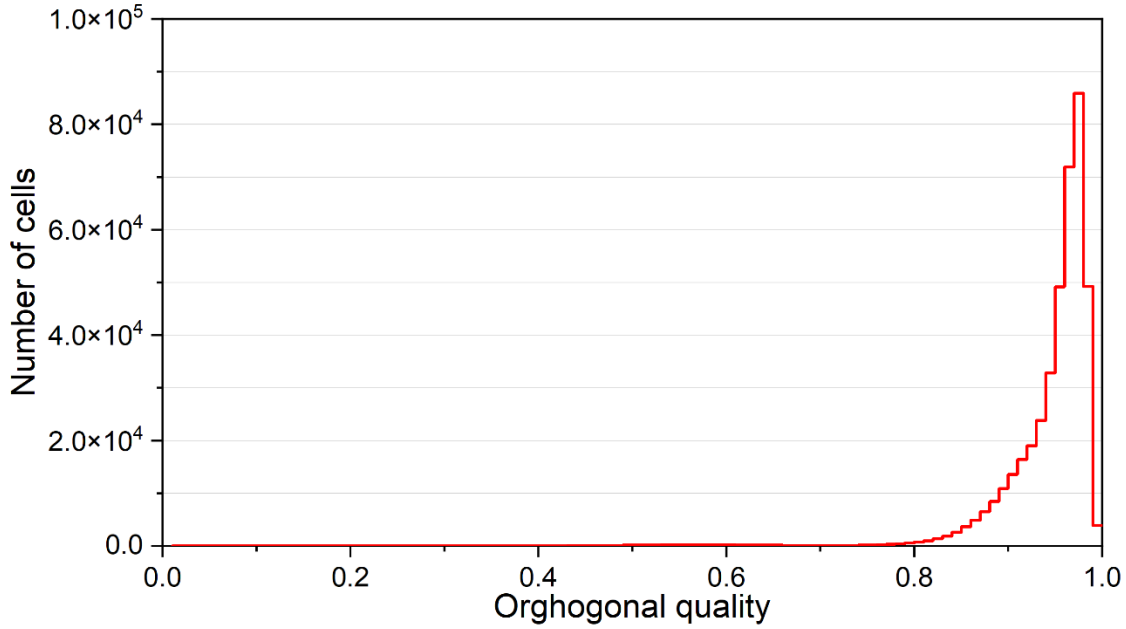

Fig. S4. Mesh elements distribution for the model without VD installation generated based on orthogonal quality.

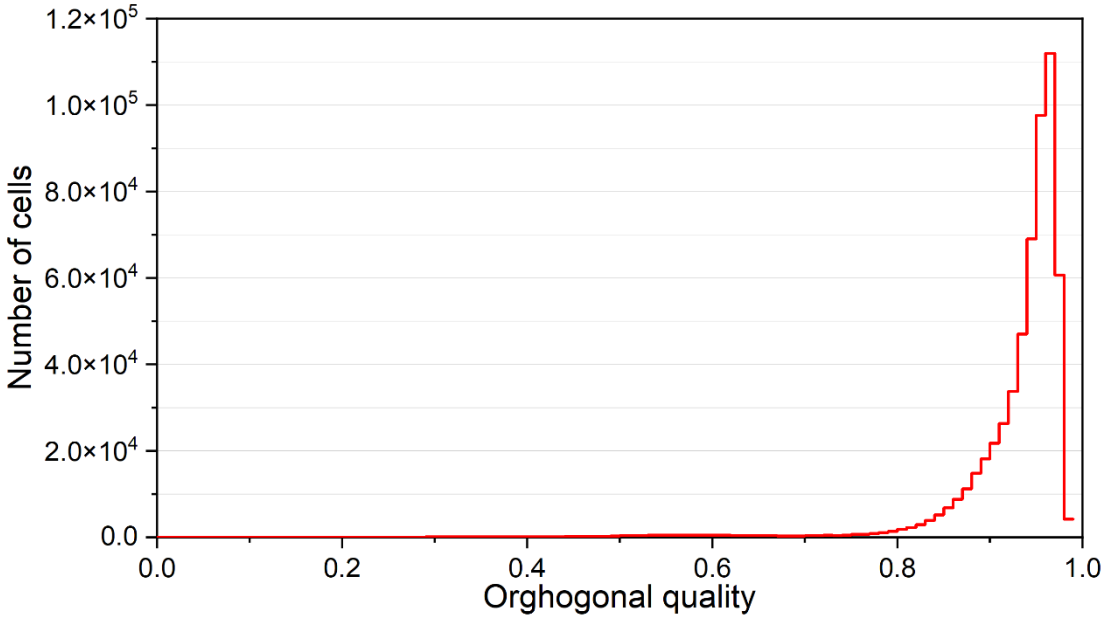

Fig. S5. Mesh elements distribution for the model with VD installation generated based on orthogonal quality.

To evaluate the effects of mesh size on CFD modeling results, a grid-independent study was conducted for the fluidized bed with VD. Figure S6 shows the coarse, medium, and fine mesh used in the evaluation. Mesh number of the coarse, medium, and fine mesh is 330, 560, and 810 thousand polyhedral meshes, respectively. The corresponding mesh size is 65, 55, and 48 times of particle size, respectively. Figure S7 shows the effects of mesh size on axial profiles of pressure and lateral profiles of CO_2 concentration ratio. It seems that mesh size has a weaker effect on the modeling results. The coarse mesh predicts a slightly higher pressure in most of the region as compared to that of fine mesh, whereas the medium mesh gives almost the same as that of the fine mesh. In addition, the coarse mesh gives a quite similar CO_2 concentration ratio profiles as that of the fine mesh. Therefore, the results confirm that the two-step EMMS/bubbling model is grid-independent model and the mesh used in this work is reasonable.

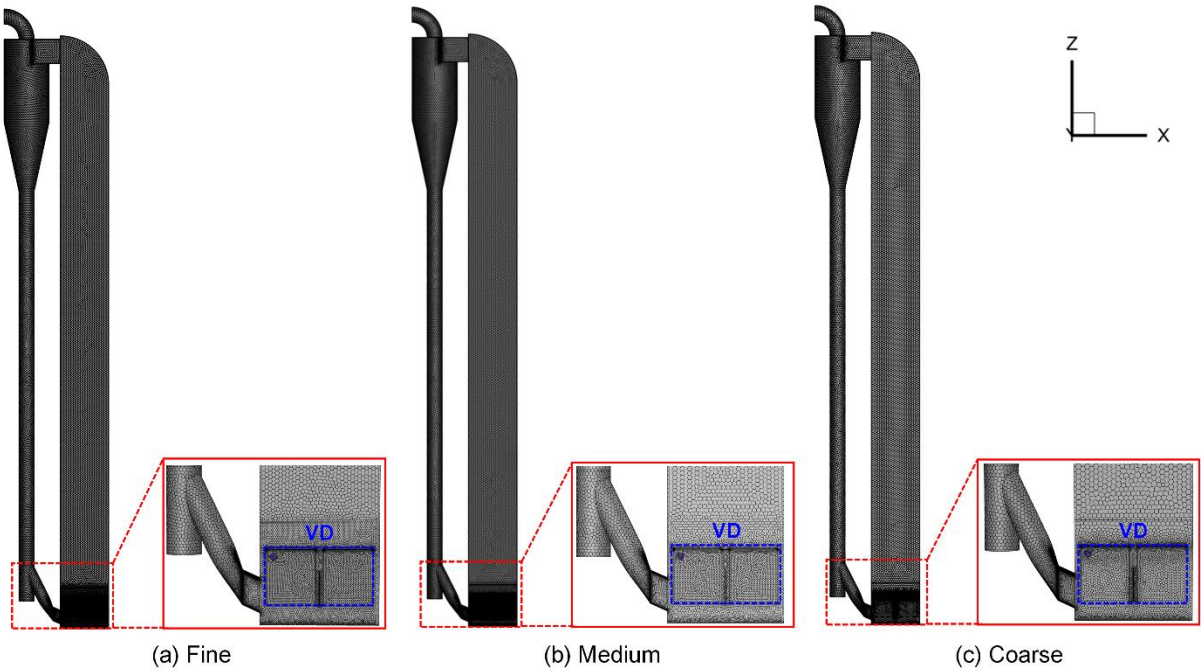

Fig. S6. Fine, medium, and coarse mesh of the fluidized bed with VD used in the grid-independent study.

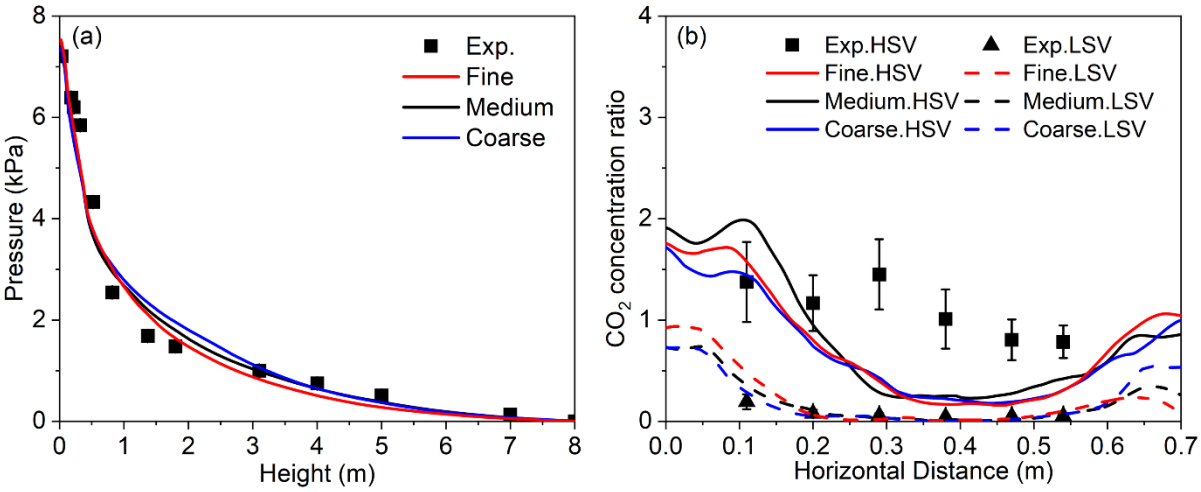

Fig. S7. The effects of mesh size on the CFD predicted axial profiles of pressure (a) and lateral profiles of CO_2 concentration ratio (b). The drag model is two-step EMMS/bubbling model. The case is U_g = 3.7 m/s and the fluidized bed is installed with VD.

4. H_D of the two-step EMMS/bubbling drag model

Figure S8 shows the contour plot of H_D of the two-step EMMS/bubbling drag model for different operating conditions. For the case of U_g = 0.94 m/s, the H_D of most of region is 1. With the increase of superficial gas velocity, the region of H_D equaled to 1 becomes small. It is also found that the H_D of operating case with high superficial gas velocity (U_g = 4.13 m/s) is

much smaller than that of low superficial velocity, as the sub-grid structure has more significance on the momentum transfer between gas and sold phase, which is consistent previous studies(Luo et al., 2017; Shi et al., 2011). To use the H_D data in the ANSYS Fluent, it is fitted as an expression of Eq. (S5).

$$H_D = a\,\mathrm{Re}_s^b \tag{S5}$$

The fitting parameters of H_D of different experiment runs are given in Table S6-S9.

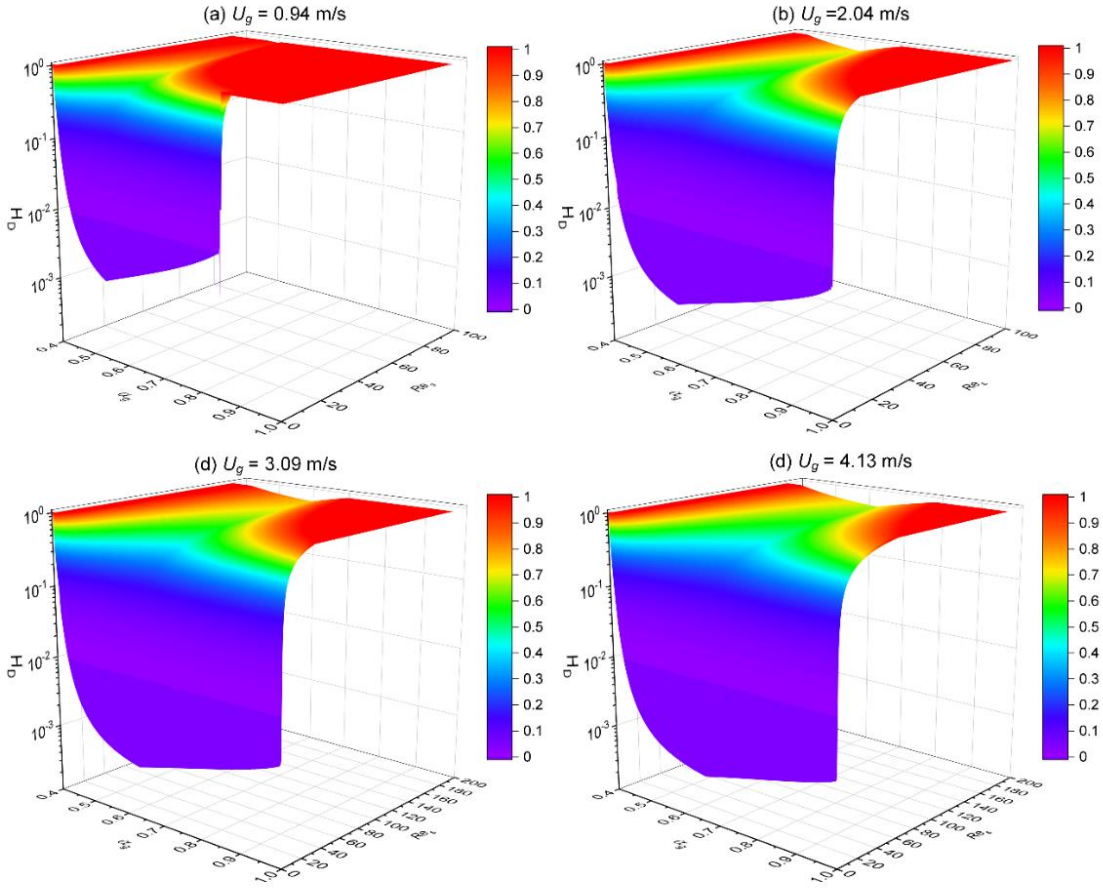

Fig. S8. Contour plot of H_D of the two-step EMMS/bubbling drag model for different operating conditions: (a) U_g = 0.94 m/s, (b) U_g = 2.04 m/s, (c) U_g = 3.09 m/s, (d) U_g = 4.13 m/s.

Table S6. Fitting correlations of H_D for U_g = 0.94 m/s.

$\begin{cases} a = -85956.3376 + 85559.7497\alpha_g - 77448.7901 \times \dfrac{\ln \alpha_g}{\alpha_g} + 22744.5396 \times \dfrac{\ln \alpha_g}{\alpha_g} + 5259.09742\alpha_{\mathrm{g}}^2 \\ b = \dfrac{\left(0.0796 + 0.5086\alpha_g - 5.5596\alpha_{\mathrm{g}}^2 + 13.1306\alpha_{\mathrm{g}}^3 - 9.1361\alpha_{\mathrm{g}}^4\right)}{\left(1.0 - 1.9998\alpha_g - 1.9758\alpha_{\mathrm{g}}^2 - 5.4355\alpha_{\mathrm{g}}^3 + 12.5680\alpha_{\mathrm{g}}^4 + 16.2183\alpha_{\mathrm{g}}^5\right)} \end{cases}$	$\left(0.4 < \alpha_{\mathrm{g}} \le 0.4405\right)$
$\begin{cases} a = 199.0447 - \dfrac{290.5809}{\alpha_g} - \dfrac{0.0029}{\alpha_{\mathrm{g}}^2} + \dfrac{228.0321}{\alpha_{\mathrm{g}}^3} - \dfrac{165.3261}{\alpha_{\mathrm{g}}^4} + \dfrac{47.7898}{\alpha_{\mathrm{g}}^5} - \dfrac{5.0940}{\alpha_{\mathrm{g}}^6} \\ b = 1981.8262 - 4117.8316\alpha_g - \dfrac{474.710}{\alpha_g} + 4269.1646\alpha_{\mathrm{g}}^2 + \dfrac{45.1439}{\alpha_{\mathrm{g}}^2} - 1767.3462\alpha_{\mathrm{g}}^3 \end{cases}$	$\left(0.4405 < \alpha_{\mathrm{g}} \le 0.5379\right)$
$\begin{cases} a = 1.7333 - 19.4571\alpha_{\mathrm{g}}^2 + 83.9359\alpha_{\mathrm{g}}^4 - 156.2620\alpha_{\mathrm{g}}^6 + 109.4721\alpha_{\mathrm{g}}^8 \\ b = 16.6326 + 111.6447\alpha_{\mathrm{g}} - 206.4298\alpha_g^2 + 148.6408\alpha_g^3 + \dfrac{3.9149}{\ln \alpha_g} \end{cases}$	$\left(0.5379 < \alpha_{\mathrm{g}} \le 0.6564\right)$
$\begin{cases} a = 3079.4054 + 5316.0819\alpha_g + 1644.5259\alpha_g^3 - 3732.1343e^{\alpha_g} + \dfrac{105.7989}{\alpha_g} \\ b = 21.8701 - \dfrac{49.7866}{\alpha_g} + \dfrac{1.6483}{\alpha_g^2} + \dfrac{75.8523}{\alpha_g^3} - \dfrac{60.1963}{\alpha_g^4} - \dfrac{0.2912}{\alpha_g^5} + \dfrac{15.1994}{\alpha_g^6} - \dfrac{4.2515}{\alpha_g^7} \end{cases}$	$\left(0.6564 < \alpha_{\mathrm{g}} \le 0.8543\right)$
$\begin{cases} a = -214.5633 + 251.8940\alpha_g \\ b = 86.7614 - 101.3840\alpha_g \end{cases}$	$\left(0.8543 < \alpha_{\mathrm{g}} \le 0.8558\right)$
$\begin{cases} a = 1 \\ b = 0 \end{cases}$	$\left(0.8558 < \alpha_{\mathrm{g}} \le 1.0\right)$

Table S7. Fitting correlations of H_D for U_g = 2.04 m/s.

$\begin{cases} a = 66567.7430 - 103583.8896\alpha_g + 626355.7747\alpha_{\mathrm{g}}^3 - 16044.1242\left(\ln \alpha_g\right)^2 + 118543.9560 \times \dfrac{\alpha_g}{\ln \alpha_g} \\ b = 33854.0917 + 36428.2234\alpha_g - 152186.6383\alpha_{\mathrm{g}}^{2.5} - \dfrac{26856.5834}{\ln \alpha_g} + \dfrac{1359.2474}{\alpha_{\mathrm{g}}^{1.5}} \end{cases}$	$\left(0.4 < \alpha_g \le 0.4299\right)$
$\begin{cases} a = 0.0702 + 0.0020\mathrm{e}^{\frac{\alpha_g - 0.4508}{0.0056}} + 0.2822\mathrm{e}^{\frac{\alpha_g - 0.4508}{0.0486}} \\ b = \dfrac{0.5208 + 1.1657\ln \alpha_g + 0.6507(\ln \alpha_g)^2}{1.0 + 2.4429\ln \alpha_g + 2.0322(\ln \alpha_g)^2 + 0.6344(\ln \alpha_g)^3} \end{cases}$	$\left(0.4299 < \alpha_g \le 0.6055\right)$
$\begin{cases} a = 1.5331 + 13.0495\alpha_g^2 - 30.2189\alpha_g^4 - 2.3841\alpha_g^6 - 6.8735\mathrm{e}^{-6}\alpha_g^8 + 433.4751\alpha_g^{10} - 1013.1760\alpha_g^{12} \\ \quad + 675.1637\alpha_g^{14} \\ b = 471.5397 + 594.4354\ln \alpha_g + \dfrac{171.5884}{\ln \alpha_g} + 65.2060\alpha_g^2 + \dfrac{30.9327}{(\ln \alpha_g)^2} - \dfrac{588.2061}{(\ln \alpha_g)^3} + \dfrac{2.2373}{(\ln \alpha_g)^3} - 421.2209\alpha_g^4 \end{cases}$	$\left(0.6055 < \alpha_{\mathrm{g}} \le 0.7298\right)$
$\begin{cases} a = 2.9687 - 17.3724\alpha_g^2 + 37.1932\alpha_g^4 - 33.1395\alpha_g^6 + 10.9825\alpha_g^8 \\ b = -38.1645 + \dfrac{129.3630}{\alpha_g} - \dfrac{164.7828}{\alpha_g^2} + \dfrac{93.5180}{\alpha_g^3} - \dfrac{19.8176}{\alpha_g^4} \end{cases}$	$\left(0.7298 < \alpha_{\mathrm{g}} \le 0.9997\right)$
$\begin{cases} a = 1 \\ b = 0 \end{cases}$	$\left(0.9997 < \alpha_{\mathrm{g}} \le 1.0\right)$

Table S8. Fitting correlations of H_D for U_g = 3.09 m/s.

$$\begin{cases} a = 18344.0785+19873.5181\alpha_g - \dfrac{9381.3151}{\alpha_g} - 100129.8707\alpha_g^2 + \dfrac{1245.0930}{\alpha_g^2} + 84371.1889\alpha_g^3 \\ b = 2791.4812 - 3189.4348\alpha_g + 13713.2485\alpha_g^{2.5} + \dfrac{2371.0733}{\ln\alpha_g} + \dfrac{-50.5128}{\alpha_g^2} \end{cases} \qquad \left(0.4 < \alpha_g \le 0.43\right)$$

$$\begin{cases} a = 15570.0701 - 0.1328\alpha_g - \dfrac{14258.2854}{\alpha_g} + 9.6317\alpha_g^2 + \dfrac{4457.8196}{\alpha_g^2} - 32896.9832\alpha_g^3 + \dfrac{5.4258}{\alpha_g^3} \\ \quad + 45957.9650\alpha_g^4 - \dfrac{278.5821}{\alpha_g^4} - 18810.8562\alpha_g^5 + \dfrac{42.3302}{\alpha_g^5} \\ b = 52.1110 + \dfrac{81.8128}{\alpha_g} - \dfrac{4.3255}{\alpha_g^2} - \dfrac{41.6201}{\alpha_g^3} + \dfrac{1.4012}{\alpha_g^4} + \dfrac{20.5058}{\alpha_g^5} - \dfrac{5.1633}{\alpha_g^6} - \dfrac{3.9120}{\alpha_g^7} + \dfrac{2.1037}{\alpha_g^8} - \dfrac{0.2869}{\alpha_g^9} \end{cases} \qquad \left(0.43 < \alpha_g \le 0.6384\right)$$

$$\begin{cases} a = -244.2913+2365.5622\alpha_g + 3881.4657\alpha_g^2\ln\alpha_g - 2158.4419\alpha_g^3 - \dfrac{2.5714}{\ln\alpha_g} \\ b = 7.5715 + \dfrac{13.3204}{\ln\alpha_g} + \dfrac{9.9624}{(\ln\alpha_g)^2} + \dfrac{3.7198}{(\ln\alpha_g)^3} + \dfrac{0.6921}{(\ln\alpha_g)^4} + \dfrac{0.0513}{(\ln\alpha_g)^5} \end{cases} \qquad \left(0.6394 < \alpha_g \le 0.7448\right)$$

$$\begin{cases} a = 7.4714+1.3248\alpha_g + \dfrac{-9.9546\mathrm{e}^{-5}}{\ln\alpha_g} + \dfrac{13.5790\ln\alpha_g}{\alpha_g} + \dfrac{6.6423}{\alpha_g^2} \\ b = \dfrac{\left(-8.5035+26.5259\alpha_g^2 - 18.8367\alpha_g^4 - 1.9385\alpha_g^6 + 2.7441\alpha_g^8\right)}{\left(1.0 - 21.3542\alpha_g^2 + 35.3522\alpha_g^4 + 29.0805\alpha_g^6 - 44.1201\alpha_g^8\right)} \end{cases} \qquad \left(0.7448 < \alpha_g \le 0.9997\right)$$

$$\begin{cases} a = 1 \\ b = 0 \end{cases} \qquad \left(0.9997 < \alpha_g \le 1.0\right)$$

Table S9. Fitting correlations of H_D for U_g = 4.13 m/s.

$\begin{cases} a = 167830.9320 - 201905.0010\alpha_g + 107839.4576\alpha_g^2 - 23228.4869 \times \dfrac{\ln\alpha_g}{\alpha_g} - \dfrac{63012.9470}{\alpha_g} \\ b = \dfrac{\left(-1.3257 + 11.0344\alpha_g - 41.2430\alpha_g^2 + 99.1351\alpha_g^3 - 153.5637\alpha_g^4 + 107.1697\alpha_g^5\right)}{\left(1.0 - 2.1087\alpha_g - 2.3877\alpha_g^2 + 1.1377\alpha_g^3 - 0.4770\alpha_g^4 + 8.1704\alpha_g^5 + 25.2704\alpha_g^6\right)} \end{cases}$	$\left(0.4 < \alpha_g \le 0.4419\right)$
$\begin{cases} a = -2436.3423 + 3141.5038\alpha_g + \dfrac{1067.5691}{\alpha_g} - 2168.0350\alpha_g^2 - \dfrac{250.8988}{\alpha_g^2} + 625.2018\alpha_g^3 + \dfrac{24.7596}{\alpha_g^3} \\ b = 807.4648 + 1381.6571\ln\alpha_g + \dfrac{280.2744}{\ln\alpha_g} + 1406.1390\alpha_g^2 + \dfrac{53.6124}{(\ln\alpha_g)^2} + 787.4953(\ln\alpha_g)^3 + \dfrac{4.3578}{(\ln\alpha_g)^3} \\ \quad + 186.5515(\ln\alpha_g)^4 \end{cases}$	$\left(0.4419 < \alpha_g \le 0.6639\right)$
$\begin{cases} a = -0.0111 - \dfrac{0.0299}{\ln\alpha_g} + \dfrac{0.0031}{(\ln\alpha_g)^2} + \dfrac{0.0016}{(\ln\alpha_g)^3} + \dfrac{0.0001}{(\ln\alpha_g)^4} \\ b = 0.3028 - \dfrac{1.3775}{\ln\alpha_g} - \dfrac{0.9932}{(\ln\alpha_g)^2} - \dfrac{0.3717}{(\ln\alpha_g)^3} - \dfrac{0.0770}{(\ln\alpha_g)^4} - \dfrac{0.0084}{(\ln\alpha_g)^5} - \dfrac{0.0004}{(\ln\alpha_g)^6} \end{cases}$	$\left(0.6639 < \alpha_g \le 0.8273\right)$
$\begin{cases} a = 7.9496 - 37.9660\alpha_g^2 + 67.6476\alpha_g^4 - 52.9850\alpha_g^6 + 15.6974\alpha_g^8 \\ b = -681.8599 - 746.5451\alpha_g + 1781.8116\alpha_g^{0.5} - \dfrac{852.0983\ln\alpha_g}{\alpha_g} - \dfrac{353.1821}{\alpha_g^2} \end{cases}$	$\left(0.8273 < \alpha_g \le 0.9967\right)$
$\begin{cases} a = 0.2709 - \dfrac{0.0002}{\ln\alpha_g} \\ b = \left(0.5236 + \dfrac{0.0001\alpha_g}{(\ln\alpha_g)^2}\right) \end{cases}$	$\left(0.9967 < \alpha_g \le 0.9997\right)$
$\begin{cases} a = 1 \\ b = 0 \end{cases}$	$\left(0.9997 < \alpha_g \le 1.0\right)$

5. The analysis of model validation error

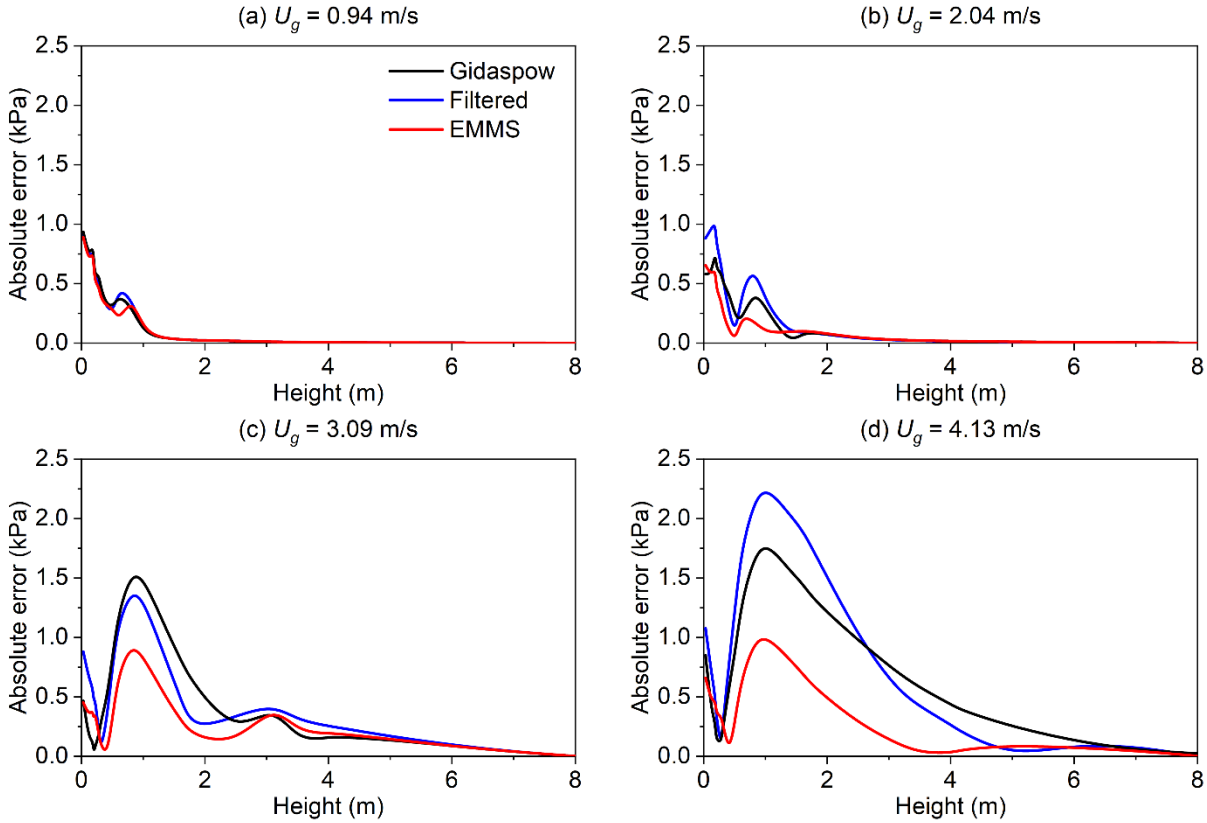

Fig. S9. Absolute error of CFD predicted pressure along height of the fluidized bed without VD under various operating conditions.

Table S10. MRE between CFD predictions and experimental measurements.

Case	U_g (m/s)	MRE of Pressure	MRE of CO_2 concentration ratio at HSV	MRE of CO_2 concentration ratio at LSV
5	0.94	17.13%	19.74%	82.75%
6	1.10	15.58%	21.39%	90.44%
7	1.27	12.55%	22.07%	88.83%
8	2.04	8.57%	19.94%	61.92%
9	3.08	12.74%	43.95%	109.61%
10	4.13	11.85%	55.43%	60.68%

Table S11. MAE between CFD predictions and experimental measurements.

Case	U_g (m/s)	MAE of Pressure (kPa)	MAE of CO_2 concentration ratio at HSV	MAE of CO_2 concentration ratio at LSV
5	0.94	0.43	0.24	0.12
6	1.10	0.40	0.25	0.24
7	1.27	0.32	0.23	0.22
8	2.04	0.21	0.22	0.09
9	3.08	0.35	0.43	0.11
10	4.13	0.36	0.61	0.05

6. Axial profiles of pressure in the VD region

Figure S10 shows the axial profiles of pressure in the VD region of the fluidized bed without and with the VD under various operating conditions. For the cases without the VD, the pressure decreases with the rising height of the fluidized bed, and it is slightly lower than the pressure in the corresponding cases with the VD, indicating that the existence of the VD increases the fluid flow resistance. For the case with U_g = 0.94 m/s, the pressure inside the VD remains the same as the one outside the VD and both decrease with the height of the fluidized bed until the height reaches 0.3 m., then the pressure inside the VD is constants as the top region inside the VD above 0.3 m is occupied by the simulated volatile together with the fluidization gas flowing from the bottom and free from solid particles as shown in Fig. S10. For the other operating conditions, simulation phenomena are observed as shown in Figs. S10 (b), (c), and (d), the start point of the pressure difference between the region of outside VD and inside VD are significantly different with that of shown in Figs. S10 (a), the pressure of outside VD is lower than that of inside VD in most of region. In addition, the height of the dense phase inside the VD is correlated with the pressure drop over the distribution holes of the VD at the height of 0.374 m, which increases with the increasing of the superficial gas velocity and simulated volatiles flow rate as shown in Fig. S10.

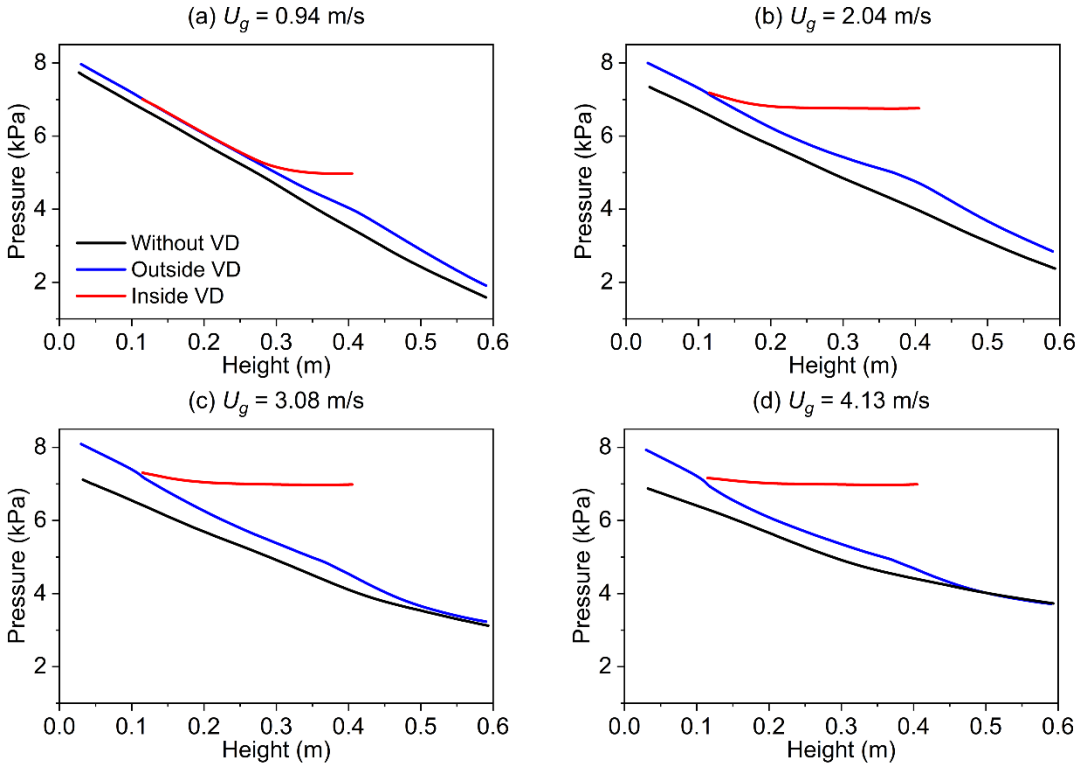

Fig. S10. Pressure axial profiles of the fluidized bed without and with the VD under various operating conditions.

Symbols

C_μ, C_1, C_2	Coefficients in turbulence model	-
d_s	Particle diameter	m
e	Restitution coefficient	-
G_K	Generated by mean velocity gradient	m^2/s^2
$\boldsymbol{g}$	Gravitational acceleration	m/s^2
g_0	Radial distribution function	
$\boldsymbol{I}$	Identity matrix	
$\boldsymbol{I}_{2D}$	Second invariant of the deviatoric stress tensor	-
$\boldsymbol{J}$	Diffusion flux	-
k	Turbulent kinetic energy	m^2/s^2
$\boldsymbol{p}$	Pressure	Pa
$\boldsymbol{P}_{friction}$	Frictional pressure	Pa
Re	Particle Reynolds number	-
S_s	Scalar filtered rates of strain	1/s
S_{Ct}	Turbulent Schmidt number	-
$\boldsymbol{u}$	Real velocity	m/s
u_{slip}	Non-dimensional slip velocity	-
u_t	Terminal velocity	m/s
V_{cell}	Mesh cell volume	m^3
Y	Mass fraction	
Greek letters		
α	Phase volume fraction	
β	Drag coefficient	$kg/(m^3 \cdot s)$
$\gamma_{\Theta s}$	Collisional dissipation of energy	m^2/s^2
ε	Turbulence dissipation rate	m^2/s^3
Θ_s	Granular temperature	m^2/s^2
λ_s	Granular bulk viscosity	Pa·s
μ	Viscosity	Pa·s
μ_t	turbulent viscosity	Pa·s
μ_s	Solids shear viscosity	Pa·s
$\mu_{s,col}$	Collisional Viscosity	Pa·s
$\mu_{s,skin}$	Kinetic Viscosity	Pa·s
$\mu_{s,fr}$	Frictional viscosity	Pa·s
ρ	Density	kg/m^3
σ_k	Prandtl numbers for k	-
σ_ε	Prandtl numbers for ε	-
$\boldsymbol{\tau}$	Stress tensor	Pa
φ	Internal friction angle	
φ_{gs}	Energy exchange between the gas and the solids phase	$kg/(m^3 \cdot s)$

Subscripts

g	Gas phase
i	Species
s	Solids phase

(Bold characters are for vectors or tensors)

Reference

ANSYS, I., 2023. ANSYS Fluent: Theory Guide, Release 2023 R1.

Krzywanski, J., Sztekler, K., Szubel, M., Siwek, T., Nowak, W., Mika, Ł., 2020a. A Comprehensive Three-Dimensional Analysis of a Large-Scale Multi-Fuel CFB Boiler Burning Coal and Syngas. Part 1. The CFD Model of a Large-Scale Multi-Fuel CFB Combustion. Entropy 22, 964.

Krzywanski, J., Sztekler, K., Szubel, M., Siwek, T., Nowak, W., Mika, Ł., 2020b. A Comprehensive, Three-Dimensional Analysis of a Large-Scale, Multi-Fuel, CFB Boiler Burning Coal and Syngas. Part 2. Numerical Simulations of Coal and Syngas Co-Combustion. Entropy 22, 856.

Luo, H., Lu, B., Zhang, J., Wu, H., Wang, W., 2017. A grid-independent EMMS/bubbling drag model for bubbling and turbulent fluidization. Chemical Engineering Journal 326, 47-57.

Shi, Z., Wang, W., Li, J., 2011. A bubble-based EMMS model for gas–solid bubbling fluidization. Chemical Engineering Science 66, 5541-5555.